

COSMICFLOWS-3

R. BRENT TULLY,

Institute for Astronomy, University of Hawaii, 2680 Woodlawn Drive, Honolulu, HI 96822, USA

HÉLÈNE M. COURTOIS

Université Claude Bernard Lyon I, Institut de Physique Nucléaire, Lyon, France

JENNY G. SORCE

Leibniz-Institut für Astrophysik, D-14482 Potsdam, Germany

ABSTRACT

The *Cosmicflows* database of galaxy distances that in the 2nd edition contained 8,188 entries is now expanded to 17,669 entries. The major additions are 2,257 distances that we have derived from the correlation between galaxy rotation and luminosity with photometry at $3.6\ \mu\text{m}$ obtained with *Spitzer Space Telescope* and 8,885 distances based on the Fundamental Plane methodology from the 6dFGS collaboration. There are minor augmentations to the Tip of the Red Giant Branch and Type Ia supernova compilations. A zero point calibration of the supernova luminosities give a value for the Hubble Constant of $76.2 \pm 3.4 \pm 2.7$ (\pm rand. \pm sys.) $\text{km s}^{-1} \text{Mpc}^{-1}$. Alternatively, a restriction on the peculiar velocity monopole term representing global infall/outflow implies $H_0 = 75 \pm 2 \text{ km s}^{-1} \text{Mpc}^{-1}$.

Key words: large scale structure of universe — galaxies: distances and redshifts

1. INTRODUCTION

Cosmicflows-3 is a compendium of galaxy distance that builds on two earlier releases (Tully et al. 2008, 2013) and draws on both original material and information from the literature. The most important original material in *Cosmicflows-3* extends the correlation between galaxy rotation and luminosity, hereafter referred to as TF (Tully & Fisher 1977), by using infrared photometry obtained with *Spitzer Space Telescope*. The most important addition from the literature is the extensive Fundamental Plane (FP) sample derived from the Six Degree Field Galaxy Survey (6dFGS) of the southern celestial hemisphere (Springob et al. 2014). Less substantial additions include new distances based on identification of the Tip of the Red Giant Branch (TRGB) in *Hubble Space Telescope* (HST) images and an update on literature distance determinations from Type Ia supernova (SNIa) observations (Rest et al. 2014; Walker et al. 2015).

The discussion will begin by describing the new *Spitzer* sample. The study involves a review of the calibration procedure, followed by application to all relevant galaxies with *Spitzer* photometry. Following that,

attention will be given to the integration of 6dFGS FP distances, heedful of the need to maintain a constant zero point scale. The next topic will visit the status of TRGB observations. Finally, similar zero-point considerations as with 6dFGS FP will guide the acceptance of SNIa information into the assembly. The SNIa calibration will be used to infer a value for the Hubble Constant at redshifts $0.05 < z < 0.6$, beyond the domain of velocity distortions.

Use will be made of a new group catalog (Tully 2015b). Associations with groups enable comparisons within and between methodologies. Large scale flow studies are improved by group averaging distances and velocities.

2. LUMINOSITY–LINEWIDTH DISTANCES WITH SPITZER PHOTOMETRY

The viability of using *Spitzer Space Telescope* photometry in a band at $3.6\ \mu\text{m}$, [3.6], to represent luminosities in the TF relation was demonstrated by Sorce et al. (2013). Photometry at $3.4\ \mu\text{m}$ with *WISE*, *Wide-field Infrared Satellite Explorer*, is similarly useful (Lagattuta et al. 2013; Neill et al. 2014). Obvious advantages of the infrared are virtual elimination of obscuration concerns and a matching to the spectral output

of the old stars that dominate the baryon mass budget. Obvious advantages of satellite observations are vastly reduced backgrounds and photometric integrity over the entire sky. A slight disadvantage compared with the familiar I band turns out to be the introduction of a color term, but the color correction required to minimize dispersion is small.

Observations with *Spitzer Space Telescope* are targeted. There have been two major programs of relevance to the current study. The first of these was S^4G , the *Spitzer Survey of Stellar Structure in Galaxies* (Sheth et al. 2010) which acquired imaging photometry in the 3.6 and 4.5 micron bands, [3.6] and [4.5], for 2352 disk galaxies at $|b| > 30^\circ$, and with distance, magnitude and size limits. The intent of the S^4G program was to study the structural properties of nearby disk galaxies (Sheth et al. 2010; Salo et al. 2015) but a substantial fraction of the S^4G sample is also of interest for this work. The second major program was our *CFS*, *Cosmic Flows with Spitzer* (Sorce et al. 2014). Only galaxies of interest for the acquisition of distances were considered in this program and observations were restricted to the 3.6 μm band. In *CFS*, a primary selection criterion was low galactic latitude, $|b| < 30^\circ$, both as a complement to S^4G and particularly because it was appreciated that it is in crowded stellar fields that *Spitzer* has the greatest advantage over the concurrent *WISE* because of superior spatial resolution. The *CFS* observations at higher latitudes favored extreme edge-on systems (Karachentsev et al. 1999), choosing among those that already have adequately observed HI line profiles.

The *Spitzer* sample encompasses observations obtained in a number of earlier programs. The relevant images are available at the *Spitzer* archive. In the interest of maintaining homogeneity, all the *CFS* and non- S^4G archival images were analyzed with the Archangel photometry package (Schombert 2007) as discussed by Sorce et al. (2012a, 2014). The integration of Archangel and S^4G photometry will be discussed in the next Section. In total, 2257 galaxy distances could be determined based on *Spitzer* photometry.

2.1. 3.6 Micron Magnitude vs. Linewidth Calibration

The calibration of the correlation between [3.6] magnitudes and HI profile widths follows previously described procedures for the calibration at I band (Tully & Courtois 2012), the *WISE* $W1$ and $W2$ bands (Neill et al. 2014), and the *Spitzer* [3.6] band (Sorce et al. 2013, 2014). The slope calibration averages over separate samples that are each approximately volume limited to specified magnitude limits and that are representative of a range of galaxy densities and dominant types.

Thirteen clusters described earlier (Tully & Pierce

2000; Tully & Courtois 2012; Neill et al. 2014) provide the slope calibration. Initially, linear fits are made to the separate samples within each cluster, with errors taken in linewidths; the so-called inverse TF relation. Then through an iterative procedure the 13 clusters are shifted in the magnitude domain to overlay on the Virgo sample with a best fit slope to the ensemble and minimized rms dispersion.

The absolute zero point is set by galaxies with distances determined by the Cepheid period-luminosity relation or the TRGB method. The Population I Cepheid distances are set by an assumed modulus for the Large Magellanic Cloud of 18.48 (Freedman et al. 2012). The Population II TRGB distances have been demonstrated to be in good agreement with the Cepheid scale (Rizzi et al. 2007). Both Cepheid and TRGB methods give distances to NGC 4258 that agree with the maser distance (Humphreys et al. 2013). It is assumed that the absolute zero point calibrators obey the same relationship as demonstrated by the 13 cluster template; ie, they randomly sample a relationship with the same slope. Minimization of the rms dispersion of the zero point calibrators with this fixed slope gives the absolute [3.6] vs. log linewidth calibration.

The important raw input, besides the absolute calibrator distances, are total [3.6] magnitudes, the linewidth estimator W_{mx} (Courtois et al. 2009, 2011), and inclinations. Minor corrections are made for reddening and velocity dependent effects. Insofar as the 13 cluster and zero point calibration are concerned there are only mild updates to the [3.6] photometry as reported by Sorce et al. (2014) and the HI linewidth values used by Neill et al. (2014). There were 291 cluster calibrators available to Neill et al. with the all-sky *WISE* coverage while only a subset of 285 are available for the *Spitzer* calibration because a few calibrators have not been targeted in any *Spitzer* program. As a consequence of minor group membership revisions discussed in Section 2.2, 305 galaxies now contribute to the 13 cluster template.

Particular attention has been given to the issue of inclinations with the present re-calibration. Uncertain inclinations are a dominant source of error. At 3.6 μm , uncertainties in reddening are minor. The larger uncertainties are projection corrections to linewidths. Historically, inclinations are derived from projected minor to major axis ratios assuming galaxies appear circular viewed face-on and have a specified thickness. Here, an edge-on disk system is assumed to have the ratio $b/a = 0.20$, with the rationale for that choice discussed by Tully & Pierce (2000).

Unfortunately, most sources of axial ratios in the literature are unreliable. Measures based on infrared photometry have proven to be un-useful, whether from *Spitzer*, *WISE*, or *2MASS*, measures by our team in-

cluded. Bulges and bars are sources of confusion. In the minority of cases observed with long integrations by *GALEX* (Morrissey et al. 2007), the resultant ultraviolet images provide reasonable isolation of disks with the virtual elimination of bulges and bars. Generally the fallback for inclination estimates is optical images, with preference for the most blueward band available.

Too often, the derivation of inclinations is not the primary concern of a photometric program, with the consequence that reported axial ratios do not realistically translate to inclinations. Inclinations were a concern of the photometry by the Cornell group and generally their axial ratios give good inclinations (Giovanelli et al. 1997; Masters et al. 2006; Springob et al. 2007). Lyon Extragalactic Database (LEDA) axial ratios are decent for inclinations if, but only if, the source is Paturel et al. (1996). The *Cosmicflows-2* compilation uses these sources as well as measurements by our collaboration. The agreement between the most reliable sources reflect uncertainties at the level of $\pm 4^\circ$.

Visual inspection can reveal instances where axial ratio measurements are misleading. On the side toward higher inclinations, galaxies manifestly viewed almost edge-on can have misrepresentative axial ratios because of bulges. These cases are generally not difficult to correct. On the side toward face-on inclinations, high surface brightness bars embedded in low surface brightness disks cause problems. Axial ratios may describe bars although the disks, if properly identified, may suggest more face-on aspects.

Ultimately, one is faced with the probability that some disk galaxies are poorly approximated by oblate spheroids. Tidal distortions, warps, strong bars, spiral features, and pronounced surface brightness transitions create confusion. With each of these problems, the manifestation to the observer depends on relative position angle and the inclination, the parameter of primary interest. From experience, roughly a third of candidates pose significant difficulties.

The strategy employed in the current study is to begin with quantitative measurements of axial ratios from photometry, comparing and often averaging over different sources (Tully et al. 2013), but then making visual evaluations. In most cases the averaged quantitative axial ratio from sources deemed reliable is considered to provide a good representation of the inclination. In cases that are considered problematic, inclinations and equivalent axial ratios are estimated visually by comparison with a trainer set of examples with reasonably established inclinations.

Our strategy is only partially satisfactory. The available imaging material is heterogeneous. Deep *GALEX* ultraviolet images are excellent but in limited supply. *Spitzer* infrared images are always available and suffi-

ciently sensitive but have unsatisfactory bulge and disk contamination. In the near future, digital area photometry of the entire sky at blueward optical bands will be available from Pan-STARRS and SkyMapper observations (Kaiser et al. 2010). Access to that material in a future *Cosmicflows* release will be appreciated because the qualitative aspects of the present procedure could produce resolution, hence distance dependent biases.

2.2. Thirteen Cluster Slope Template

The individual fits to 13 clusters are not very different from previous fits shown in Sorce et al. (2014). The *Spitzer* photometry and HI linewidth information is essentially the same. A new study of galaxy groups (Tully 2015b) has led to some modifications. Spatial and velocity associations between the *Spitzer* sample and the 13 calibration clusters have led to the identification of 26 additional cluster members with appropriate properties. The group analysis resulted in a split of the Abell 1367 Cluster into two components (nest 100005 is A1367 and nest 120005 is displaced by 2° and lies slightly closer). The new calibration uses 17 galaxies associated with the revised A1367. In all, the new calibration uses 305 galaxies, an increase from 287 in Sorce et al. (2014). In the particular case of the Virgo Cluster, we continue to only use galaxies across a restricted spatial domain that should minimize background contamination. This issue is re-evaluated in Section 6.1 once the calibration is completed and applied to the full *Spitzer* sample. In this new work, the greatest cause for changes comes from revised inclinations. Figure 1 shows the new *Spitzer* [3.6] vs. linewidth correlation for 13 clusters shifted to an optimal fit at the distance of the Virgo Cluster.

The infrared TF correlation has a color term (Sorce et al. 2013, 2014; Neill et al. 2014). An adjustment that reduces scatter can be made if the $I - [3.6]$ color is available. The color adjustment is only slightly different from the earlier formulation. Now:

$$\Delta[3.6] = -0.55(I - [3.6] + 1). \quad (1)$$

Application of the color term subtly but significantly improves the infrared TF correlation. The color corrected version of Figure 1 is shown as Figure 2. Here, for the 15 calibrator galaxies lacking I magnitudes the color adjustment is taken to be zero. The slope without color adjustment is -9.72 ± 0.19 and after color adjustment is -9.16 ± 0.17 .

As noted in Sorce et al. and Neill et al. there is a small selection bias that becomes increasingly important at distances where the faintest galaxies in a sample have intrinsic magnitudes near M^* , characterizing the exponential cutoff of the Schechter function (Schechter 1976). The current sample closely approximates the Neill et al. sample and the bias adjustments advocated in that pa-

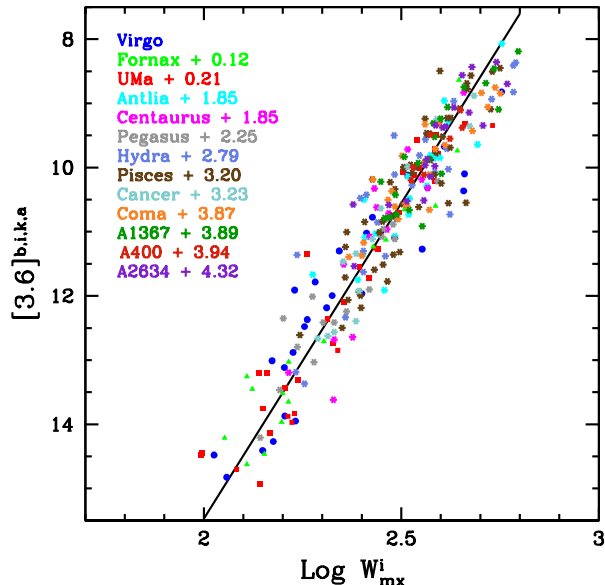


Figure 1. $[3.6]$ vs. HI linewidth template using samples drawn from 13 clusters and shifted to a best fit at the relative distance of the Virgo Cluster. Colors distinguish the 13 separate clusters. The rms scatter is 0.55 mag.

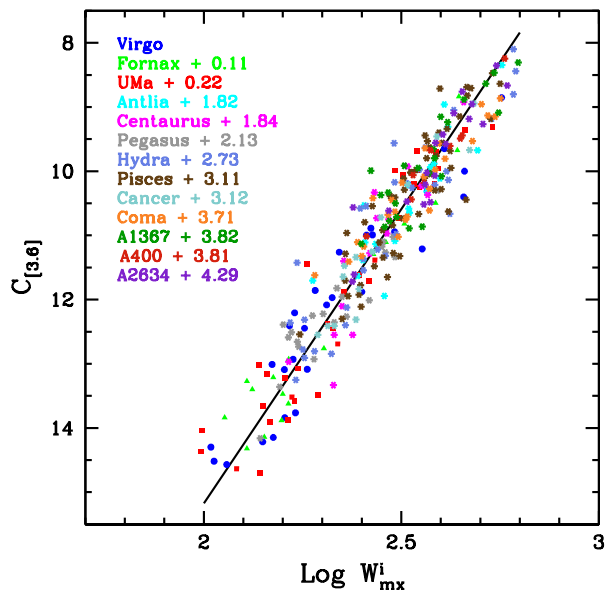


Figure 2. Color corrected version of the $[3.6]$ vs. HI linewidth template. Scatter 0.48 mag.

per are incorporated in this work.

2.3. Zero Point Calibration

The absolute scale of the TF relations is set by nearby galaxies with alternate distance estimates that are considered the best available. Here, 33 of the 37 galaxies considered by Neill et al. (2014) provide the calibration. Three of the Neill et al. calibrators lack *Spitzer* photometry (M33, NGC 3109, NGC 4945) while one

(NGC 4535) is given a revised inclination that fails our 45° limit. The input distances are derived in 25 cases from the Cepheid period-luminosity relation assuming a fiducial distance modulus for the Large Magellanic Cloud of 18.48 (Freedman et al. 2012; de Grijs et al. 2014), in 19 cases from the TRGB method assuming the calibration by Rizzi et al. (2007), and in the special case of NGC 4258 from the geometric model of the maser emission (Humphreys et al. 2013). The calibration of the Population I Cepheids and Population II red giant branch tip are independent, yet give distances that agree at the level of 0.01 mag. Eleven galaxies have both Cepheid and TRGB measures. The Cepheid, TRGB, and maser methodologies agree on the distance to NGC 4258 of 7.57 ± 0.10 Mpc.

The sample of galaxies with well established distances does not approximate a volume limited sample so should not be used to define the slope of the dependency between rotation rate and luminosity. The slope is defined by the 13 cluster template. Assuming that slope, the known absolute luminosity and inclination corrected line width of each of the 33 absolute calibrators provides an independent zero point estimation. The rms minimized deviation for the 33 galaxies provides the best fit solution.

This procedure was carried out separately for the basic $[3.6]$ vs. linewidth correlation and for the color adjusted version. The calibrations are

$$M_{3.6}^{b,i,k,a} = -20.35 \pm 0.09 - 9.72 \pm 0.19 (\log W_{mx}^i - 2.5) \quad (2)$$

$$M_C = -20.38 \pm 0.08 - 9.16 \pm 0.17 (\log W_{mx}^i - 2.5) \quad (3)$$

where W_{mx}^i are inclination corrected linewidths, $M_{3.6}^{b,i,k,a}$ are absolute magnitudes in the *Spitzer* $[3.6]$ band corrected for absorption within our Galaxy and the host galaxy, for translation of the rest frame with respect to the filter response and an aperture correction (Sorce et al. 2013), and M_C is the color adjusted modification of $M_{3.6}^{b,i,k,a}$. The rms dispersions of the absolute calibrators from these relations are ± 0.54 for the basic correlation and ± 0.45 for the color adjusted version.

Statistics on the cluster fits are assembled in Table 1. Distances are provided alternatively with, and without, color corrections. The differences are not statistically significant but uncertainties are slightly reduced through the color adjustment and color adjusted distances are preferred. The table also includes the cluster distances determined in the *WISE* $W1$ band at $3.4 \mu\text{m}$ by Neill et al. (2014), our most recent previous calibration. The Neill et al. cluster distances are on average 3% greater. The newly added galaxies to the cluster template sample have a slight tendency to lie to the low linewidth side of the mean TF relation on average, some-

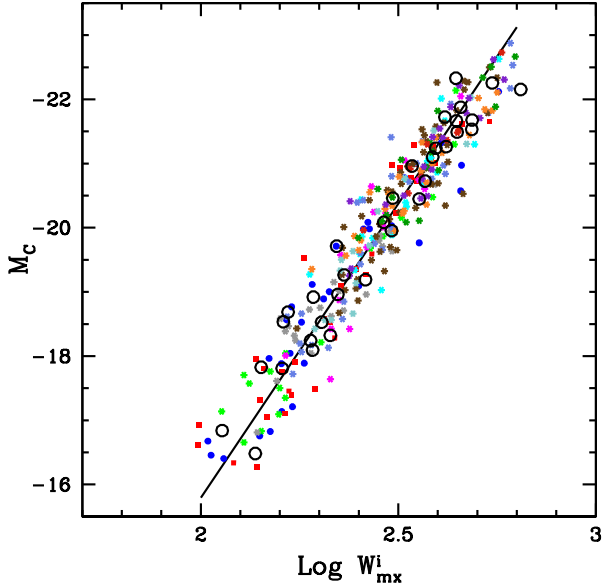


Figure 3. Color corrected absolute [3.6] luminosity vs. HI linewidth correlation. Absolute luminosity scale is set by 33 galaxies identified by large open circles. Zero-point scatter is 0.45 mag.

thing taken to be a statistical vagary but which lowers distances and increases the calculated H_0 . The difference from the Neill et al. calibration is less than the 1σ error on the color corrected zero point, Eq 3.

Table 1. Template Cluster Distances

Cluster	μ_{cc}	\pm	b	μ_{uc}	\pm	V_{mod}	d_{cc}	err	d_{uc}	err	d_{W1}	H_i
Virgo	31.029	0.136	0.000	30.908	0.164	1495	16.1	1.0	15.2	1.2	16.2	93.1
UrsaMajor	31.182	0.120	0.000	31.123	0.138	1079	17.2	1.0	16.8	1.1	17.2	62.6
Fornax	31.099	0.148	0.000	31.029	0.169	1358	16.6	1.2	16.1	1.3	17.5	81.9
Antlia	32.835	0.140	0.040	32.800	0.154	3198	36.9	2.4	36.3	2.7	39.0	86.7
Centaurus	32.808	0.168	0.000	32.756	0.191	3823	36.4	2.9	35.6	3.3	38.5	104.9
Pegasus	33.211	0.132	0.000	33.162	0.148	3062	43.9	2.8	42.9	3.0	44.0	69.8
Hydra	33.714	0.154	0.010	33.711	0.176	4088	55.3	4.1	55.2	4.7	62.1	73.9
Pisces	34.105	0.104	0.020	34.130	0.122	4759	66.2	3.3	67.0	3.9	68.3	71.9
Cancer	34.149	0.125	0.020	34.155	0.148	5059	67.6	4.0	67.8	4.8	64.2	74.9
Coma	34.792	0.118	0.040	34.818	0.141	7370	90.9	5.1	92.0	6.2	93.9	81.1
A1367	34.863	0.121	0.080	34.879	0.143	6969	93.9	5.4	94.6	6.4	98.1	74.2
A400	34.950	0.115	0.110	34.957	0.134	7228	97.7	5.3	98.0	6.2	100.0	74.0
A2634/66	35.347	0.123	0.079	35.309	0.143	8938	117.3	6.8	115.3	7.9	116.9	76.2

NOTE— μ_{cc} and μ_{uc} are color corrected and uncorrected distance moduli respectively (mags); d_{cc} and d_{uc} are corresponding distances (Mpc); d_{W1} is distance (Mpc) from Neill et al. (2014); V_{mod} (km s^{-1}) and H_i ($\text{km s}^{-1} \text{Mpc}^{-1}$) are defined in Eq. 5.

2.4. Field Sample

Distances are estimated for 2257 galaxies. These galaxies meet the following criteria: (i) measured linewidths with uncertainties $\leq 20 \text{ km s}^{-1}$, (ii) satisfac-

tory *Spitzer* [3.6] photometry, (iii) morphological types Sa and later, (iv) inclinations more edge-on than 45° , (v) HI not confused by an adjacent system, and (vi) not morphologically disrupted or peculiar. The last criterion is subjective; we tend to be inclusive.

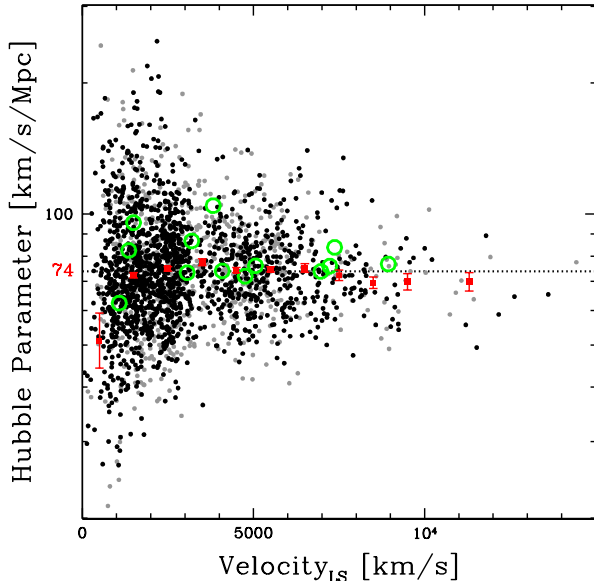


Figure 4. Hubble parameter $H_i = V_{mod}^i/d_i$ for the full *Spitzer* sample. Distances from the color adjusted relation are black while distances from the basic correlation (ie, lacking *I* band magnitudes for the color adjustment) are in grey. Averages of H_i in 1000 km s^{-1} intervals are plotted in red with 1 standard deviation errors. The average for 647 values of H_i with $V_{LS} > 4000 \text{ km s}^{-1}$ is $73.6 \text{ km s}^{-1} \text{ Mpc}^{-1}$. Large green circles identify the Hubble parameter values for the 13 template clusters.

Distances require correction for a minor selection bias. The bias is minimized by using the inverse TF relation with errors taken in linewidth (Willick 1994) but a small bias persists because there are more faint galaxies available to scatter brightward than bright galaxies to scatter faintward. The present cluster calibration samples are almost identical to those used in the Neill et al. (2014) study in the *WISE* $3.4 \mu\text{m}$ band and the bias correction is taken to be the same.

$$b = 0.004(\mu - 31)^{2.3} \quad (4)$$

where b is the bias correction and μ is a measured distance modulus. For $\mu \leq 31$, $b = 0$.

Evaluation of individual Hubble parameters, $H_i = V_i/d_i$, where V_i and d_i are measured velocities and distances, provides a way of identifying aberrant measurements. Here, the velocity in the Hubble parameter is in the CMB frame modified by cosmological curvature terms

$$H_i = V_{mod}^i/d_i = \frac{cz_i}{d_i} \left\{ 1 + \frac{1}{2}[1 - q_0]z - \frac{1}{6}[1 - q_0 - 3q_0^2 + j_0]z^2 \right\} \quad (5)$$

where z_i is redshift, the jerk parameter $j_0 = 1$ and the acceleration parameter $q_0 = \frac{1}{2}(\Omega_m - 2\Omega_\Lambda) = -0.595$ (taking $\Omega_m = 0.27$, $\Omega_m + \Omega_\Lambda = 1$).

Cases with H_i that deviate by $> 3\sigma$ from the mean

were examined. In a majority of such cases, the target could be seen in retrospect to fail our selection criteria and could be removed from the sample. However there were cases with no evident anomaly. Indeed, it has been long known that about 3% of candidates have excursions greater than 3σ from the TF relation, some reaching $4 - 5\sigma$, statistically improbable if the errors are Gaussian. The situation is the same with the current sample. It is to be appreciated that large deviations from the mean can be physically realistic for very nearby systems where true peculiar velocities can dominate over errors. After due consideration for this possibility, galaxies with deviations in H_i greater than 3.7σ are rejected. Figure 4 shows the distribution of H_i with systemic velocity for the accepted sample.

It is seen that the *Spitzer* sample is dense at velocities less than 3000 km s^{-1} , then falls off, but picks up again through 7000 km s^{-1} , then rapidly falls off. This behavior is a result of mixing two selection criteria. There are many targets at $V < 3000 \text{ km s}^{-1}$ as a reflection of the upper distance limit of the *S⁴G* sample and the intent of our *CFS* program to supplement *S⁴G* at Galactic latitudes below 30° . Then at higher velocities the sample is dominated by extreme edge-on galaxies from Karachentsev et al. (1999). These galaxies have very low axial ratios, hence have small bulges, hence are typically Sc spirals. Targets were selected that already had well observed HI profiles. The number observed was governed by the restricted availability of *Spitzer* observing time.

In Figure 4, distances estimated from the color adjustment formula, Eq. 3, lead to the black points while the uncorrected distances through Eq. 2 lead to the grey points. Average values of the Hubble parameter, V_{mod}^i/d_i , in 1000 km s^{-1} bins are shown in red with standard deviations of the mean. Values for the 13 template calibrator clusters are shown by large open green circles. Large excursions of the Hubble parameter are seen at low velocities where peculiar velocities are significant. Averaging in the modulus over 647 galaxies with $V_{LS} > 4000 \text{ km s}^{-1}$ gives $\langle H_i \rangle = 73.6 \pm 7 \text{ km s}^{-1} \text{ Mpc}^{-1}$.

3. SIX DEGREE FIELD GALAXY SURVEY DISTANCES

Springob et al. (2014) have published a sample of great importance for velocity field studies. They have combined measures of the central velocity dispersion of galaxies obtained in the course of the eponymous Six Degree Field Redshift Survey (Jones et al. 2009) with photometry from 2MASS, the Two Micron All-Sky Survey (Jarrett et al. 2000), to derive distances from the FP correlation (Djorgovski & Davis 1987; Dressler et al. 1987). They give distances for 8885 galaxies within $16,000 \text{ km s}^{-1}$, all in the south celestial hemisphere.

The accuracy for each measure is $\sim 25\%$. Details regarding the observed parameters and the fundamental plane fitting are discussed by Magoulas et al. (2012) and Campbell et al. (2014).

The 6dFGS sample is of particular interest because coverage of the celestial south had previously been deficient. The most sensitive radio telescopes are in the north, leading to an imbalance in coverage with the TF method. Inclusion of the 6dFGS sample roughly doubles the number of galaxies with measured distances within $z = 0.1$ and provides superior all-sky inclusiveness within $16,000 \text{ km s}^{-1}$.

Springob et al. (2014) provide distances as a fraction of the distance the galaxies would have if they obey the Hubble law. The angular diameter distances that are the natural product of an FP analysis were converted to co-moving distances by Springob et al. and are further converted to luminosity distances here, consistent with our other measures: $d_L = (1+z)d_c$ where d_L and d_c are luminosity and co-moving distances respectively and z is redshift. It remains only to establish a zero-point match between the 6dFGS data and the other elements of our catalog.

As an initial scaling, to be roughly but not exactly consistent with the zero-point of the rest of our sample, a global expansion value of $75 \text{ km s}^{-1} \text{ Mpc}^{-1}$ was assumed for 6dFGS. We confirm that the scatter in distances reflected in the scatter of the individual Hubble parameter measures is the advertised 26%. For 112 galaxies in 26 6dFGS groups that are in common with the *Cosmicflows-2* compilation, there is agreement in distance moduli on average, within 1σ . The dispersions about the mean group distance moduli are as anticipated: for 8 groups with 6 – 10 measurements (60 galaxies total) the 6dF rms is ± 0.50 , while for the same galaxies in *Cosmicflows-2*, the rms is ± 0.42 .

Here are modulus comparisons between 6dFGS at the fiducial scale $H_0 = 75$ and *Cosmicflows-2* by source of the CF2 distance.

SNIa (15 cases): $\langle \mu_{6df} - \mu_{cf2} \rangle = -0.03 \pm 0.19$ with scatter ± 0.74

SBF (35 cases): $\langle \mu_{6df} - \mu_{cf2} \rangle = -0.11 \pm 0.08$ with scatter ± 0.50

FP (34 cases): $\langle \mu_{6df} - \mu_{cf2} \rangle = 0.14 \pm 0.06$ with scatter ± 0.35

TF (76 cases): $\langle \mu_{6df} - \mu_{cf2} \rangle = -0.55 \pm 0.07$ with scatter ± 0.57

All but TF (84 cases): $\langle \mu_{6df} - \mu_{cf2} \rangle = 0.00 \pm 0.05$ with scatter ± 0.48

There is statistical agreement with all but the TF comparisons. The issue is pursued in Figure 5. The cloud of grey points represent the entire 6dFGS sample of 8885 galaxies tied to a fiducial $H_0 = 75 \text{ km s}^{-1} \text{ Mpc}^{-1}$ zero-point. The average of the 8668 cases above 4000 km s^{-1} ,

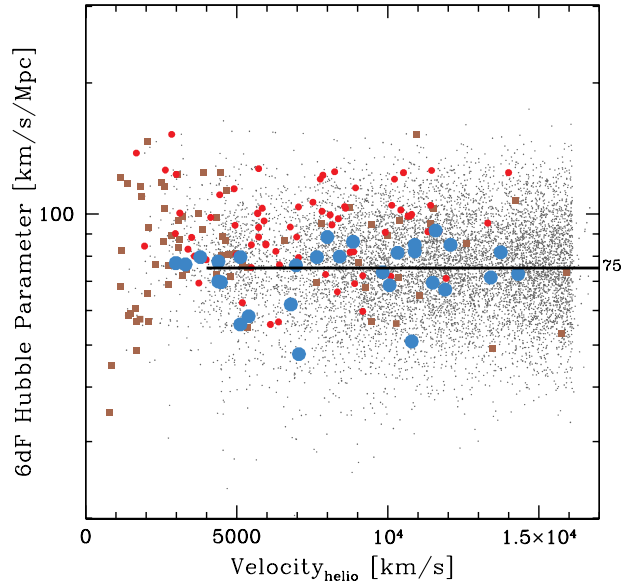


Figure 5. Hubble parameter, V_{mod}/d , for sub-samples. The full 6dFGS sample is represented by small grey dots, with the distance scale set by the choice $H_0 = 75 \text{ km s}^{-1} \text{ Mpc}^{-1}$. The average value for galaxies with $V_{helio} > 4000 \text{ km s}^{-1}$ is $75 \text{ km s}^{-1} \text{ Mpc}^{-1}$. The large blue points represent mean values for 29 groups with 6dFGS distances. The brown and red points represent the values for individual galaxies within the 6dFGS sample that also have alternative distance estimates: brown squares if SNIa, SBF, or, FP; red circles if TF.

the domain relatively uncontaminated by peculiar velocities, is $75 \text{ km s}^{-1} \text{ Mpc}^{-1}$. The group comparisons (blue circles) and individual comparisons involving SNIa, SBF, and FP alternatives (brown squares) are consistent with the fiducial input of $75 \text{ km s}^{-1} \text{ Mpc}^{-1}$. The red circles representing comparisons with TF lie systematically high; the 6dFGS distances appear to be too small in these cases.

The galaxies in the 6dFGS – TF overlap are overwhelmingly spirals; 80% have 6dFGS spiral morphologies and all meet the type Sa or later criterion of the TF sample. The indication of an anomaly in the spiral component of the 6dFGS FP distances compels a closer look. The 6dFGS collaboration provide a numerical morphological type for each of the galaxies in their sample, running from $M_t = 0$ for ellipticals, through $M_t = 2$ for lenticulars, to $M_t = 4$ for spirals (Campbell et al. 2014). We calculate the Hubble parameter for the individual galaxies in the 6dFGS sample, $H_i = V_i/d_i$ where the velocity is a group average if possible, and then we average the Hubble parameter values in M_t bins.

The resultant means and 1σ standard deviations are displayed in Figure 6. There is an unambiguous trend for values of H_i to increase with increasing M_t , implying distances are measured relatively too close with increasing M_t . The trend is reasonably captured by the red

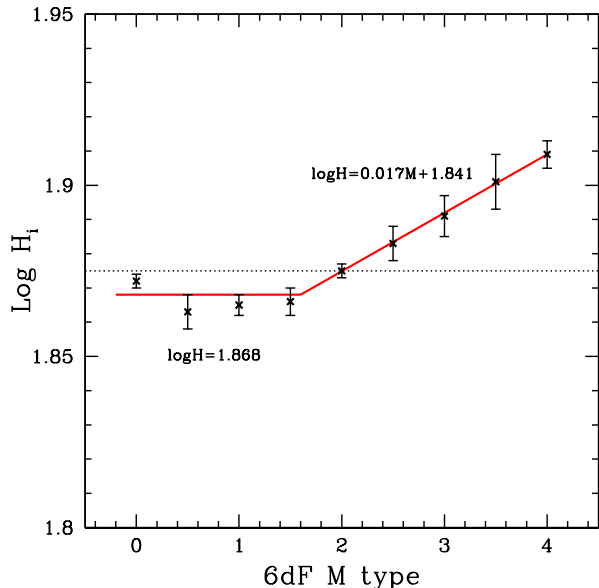


Figure 6. Mean values of the Hubble parameter for 6dFGS galaxies with velocities greater than 4000 km s^{-1} binned by 6dFGS morphological M type. The fiducial setting for the sample is $H_0 = 75 \text{ km s}^{-1} \text{ Mpc}^{-1}$ identified by the horizontal dotted line. The solid red lines describe statistical deviations from the fiducial value as a function of M type.

lines in the figure, with mean H_i constant at $M_t \leq 1.6$ and increasing at $M_t > 1.6$. These fits with a break at $M_t = 1.6$ translate to corrections in distance moduli. The adjustments slightly affect the modulus comparisons with the CF2 scale discussed earlier in this section. Minimization of the offset with the 84 galaxies with SNIa, SBF, or FP distances on the CF2 scale requires reducing 6dFGS galaxy moduli by 0.007 mag from the fiducial scale set by $H_0 = 75$. This minor offset is combined with the type correction in our formulation of adjustments to 6dFGS distances to optimize the linkage to the CF2 scale:

$$\mu_{6df}^c - \mu_{6df}^{fid} = -0.042 + 0.085(M_t - 1.6) \quad (6)$$

if $M_t > 1.6$ and

$$\mu_{6df}^c - \mu_{6df}^{fid} = -0.042 \quad (7)$$

if $M_t \leq 1.6$, where μ_{6df}^c and μ_{6df}^{fid} are corrected and fiducial ($H_0 = 75$) distance moduli.

The FP and TF correlations have related physical origins. The TF method is based on the assumption that rotation dominates the kinematics as is generally justified in mainly disk systems while the FP method is based on the assumption that dispersion dominates kinematics as found in early-type systems and bulges. Bulge/disk type dependencies can be expected in FP and TF correlations. With the Spitzer TF calibration the color term is a proxy for type. There have been

attempts to find unification correlations, linking luminosities, dimensions, and kinematics across galaxy types (Zaritsky et al. 2011; Cortese et al. 2014).

4. TIP OF THE RED GIANT BRANCH DISTANCES

Imaging that resolves stars in nearby galaxies with *Hubble Space Telescope* is ongoing, both by members of our collaboration and by others. Regardless of the source, the archival images are analyzed by our team in a coherent fashion (Makarov et al. 2006; Rizzi et al. 2007; Jacobs et al. 2009) as reviewed in *Cosmicflows-2* (Tully et al. 2013). That earlier release contained 297 TRGB distances while here the number has grown to 384, a 29% increase.

Currently roughly half of known galaxies brighter than $M_B = -12$ suspected to be within 10 Mpc have TRGB distances. Interesting subsamples or individual targets have been discussed in separate publications (Karachentsev et al. 2014b,a, 2015b,a; Tully et al. 2015). The methodology has been extended to the infrared, where the TRGB is bright and Galactic reddening is diminished (Dalcanton et al. 2012; Wu et al. 2014).

Figure 7 provides an example of a TRGB measurement with *Hubble Space Telescope* data. In this case, there are prominent Pop I features in the main sequence at color F606W-F814W ~ 0 and the red supergiant column at F814W < 25 at F606W-F814W ~ 1 , and an abundance of intermediate age asymptotic giant branch stars above the TRGB. The red giant branch itself is widened by metallicity and age mixing. Nevertheless, the TRGB is defined at the level of 5% in magnitude. The fit is made with a maximum likelihood algorithm that incorporates the evaluation of superposed fake stars to determine completion and measurement uncertainties (Makarov et al. 2006). A weak metallicity–age dependent color term is applied (Rizzi et al. 2007). As a guide to the eye, the tick marks are at intervals of 0.2 on the magnitude scale, steps of 10% in distance.

Knowledge of so many TRGB distances has been transformative. Uncertainties in these distances are at the level of 5%. Group affiliations are unambiguous. Meaningful measures can be made of individual peculiar velocities, $V_{pec} = V_{obs} - H_0 d$. Here, V_{obs} is the observed velocity and the cosmic expansion expectation velocity is the product of the Hubble Constant, H_0 , and distance d . At 10 Mpc an uncertainty of 5% in distance transforms to an uncertainty in V_{pec} of less than 40 km s^{-1} , considerably less than deviant motions of a few hundred km s^{-1} seen above and below the supergalactic plane and toward the Virgo Cluster (Tully et al. 2008; Karachentsev et al. 2014b, 2015b).

5. TYPE IA SUPERNOVA DISTANCES

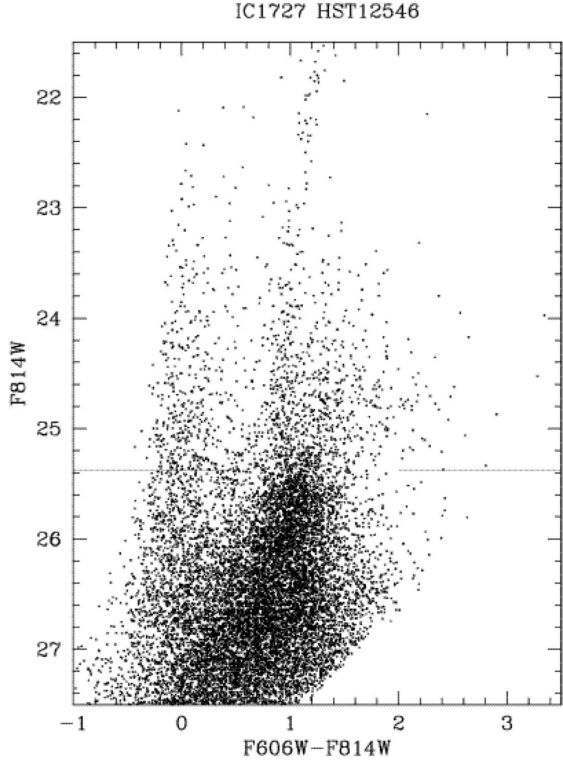


Figure 7. Color-magnitude diagram for IC 1727. The horizontal dashed line lies at the magnitude of the tip of the red giant branch and indicates a distance of 7.5 Mpc.

Peculiar velocity uncertainties associated with a particular methodology grow linearly with redshift. Uncertainties from Type Ia supernova (SNIa) measurements are at least a factor 2 less than those from the TF or FP estimates, so each one is four or more times as valuable. Indeed, at velocities greater than $10,000 \text{ km s}^{-1}$ to the $30,000 \text{ km s}^{-1}$ limit of this catalog, SNIa are making an increasingly dominant contribution.

Cosmicflows-2 contained 309 SNIa distances from five sources, with *Union-2* (Amanullah et al. 2010) as backbone. The most important new contribution is provided by Rest et al. (2014). Restricting to $z < 0.1$, this new sample contains an overlap of 141 SNIa with our earlier compilation and 58 new cases. The substantial overlap provides a robust zero-point translation of Rest et al. distance moduli to the *Union-2* sample on the CF2 zero-point scale, $\mu_{union2}^{cf2} = \mu_{rest} - 0.167 (\pm 0.007)$. The r.m.s. scatter between old and new measures is a satisfactory ± 0.079 , 4% in distance. The zero point offset found for the 141 SNIa in common with *Cosmicflows-2* is then applied to the 58 additional objects studied by Rest et al.

Walker et al. (2015) provide material for 29 additional distances to SNIa within $z = 0.1$. The cases are all new so the zero-point match is less constrained. Walker et al. assert that their zero-point is set by the choice $H_0 = 70.8 \text{ km s}^{-1} \text{ Mpc}^{-1}$, which is consistent with the distances we derive from the parameters they provide. Our input zero-point is consistent with $H_0 = 74.4 \text{ km s}^{-1} \text{ Mpc}^{-1}$ (Neill et al. 2014). Consequently, we decrease the Walker et al. distances by a factor 0.952, or 0.108 in the modulus.

While no direct comparison can be made with an alternative distance estimate to a host galaxy for this sample, a check of our proposed rescaling is afforded by events that have occurred in two groups with alternative distance estimates. In the case of the NGC 5044 Group, nest 100019 in Tully (2015b), one surface brightness fluctuation and three TF distances have a weighted average modulus of 32.56, in excellent agreement with the rescaled modulus of 32.63 for supernova 2013aiz in ESO 576-017. However the situation is perplexing in the case of Abell 539 where the earlier supernova 2004ge (Folatelli et al. 2010) along with 10 TF and 25 FP (plus two measures in the current *Spitzer* sample) are in good agreement at a modulus 35.29, with formal 95% uncertainty ± 0.12 (the modulus for 2004ge alone is 35.28). The Walker et al. supernova 2011pn, at modulus 35.68 is statistically consistent. Supernova 2011ot, at 36.12, is unexpectedly deviant. While better agreement could be forced with an unseemly large adjustment to the Walker et al. scale, the substantial difference between the 2011ot and 2011pn moduli would remain. It seems best to not place too much weight on individual measurements.

While the relative distances of the 29 systems in the Walker et al. sample are expected to be of similar high quality as other SNIa measures, the zero-point linkage is subject to uncertainty at the level of $\sim 5\%$. With the addition of material from the two new literature sources, we now have 391 SNIa distances within $z = 0.1$. We need to check if the minor revisions of the TF calibration have slightly changed the zero point of the SNIa scale, but before giving attention to that issue there is one more improvement to discuss.

6. GROUP CATALOG

Averaging over groups reduces uncertainties in both distances and velocities. In the case of velocities, the averaging can include *all* known group members, not just the relatively few with measured distances. The ensuing advantage is particularly evident in the case of rich clusters with large velocity dispersions.

In the case of distances the interests are three-fold. There is the clear advantage of reducing distance uncertainties. Also, integrating over many groups, com-

parisons between methods constrain zero-point offsets. And multiple measures within a group serve to isolate egregiously discordant distance estimates.

The group catalog used with the construction of *Cosmicflows-2* was poorly defined. A new catalog (Tully 2015b) is more rigorous. The input for the new group catalog is the 2MASS Redshift Survey (2MRS) sample of 43,526 galaxies brighter than $K_s = 11.75$ (Huchra et al. 2012). This sample strongly overlaps the 6dFGS sample, the latter extending to a fainter 2MASS limit but only in the celestial south. The 2MRS $K < 11.75$ sample peaks in numbers by 10,000 km s^{-1} but extends to beyond the 6dFGS cutoff of 16,000 km s^{-1} .

Three-quarters of the galaxies in the present collection of distances associate with groups (called “nests”) in the catalog of Tully (2015b). The linkages are either direct galaxy matches or indirect fits to spatial and velocity criteria. In the latter cases the criteria are specified by the total 2MASS K -band luminosities of the groups, corrected for missing light with distance. The integrated group luminosities predict expectation velocity dispersions, σ_p , and virial dimensions characterized by the radius of second turnaround, R_{2t} . Group linkages are contemplated if velocities are within $3\sigma_p$ of the group mean and projected locations are within $1.5R_{2t}$. As a second step, linkages are rejected if *both* velocities deviate by greater than $2\sigma_p$ of the mean and locations are outside $1.0R_{2t}$. Accordingly, 6348 of 8198 galaxies in the old *Cosmicflows-2* are linked to nests (77%), 6157 of 8885 galaxies in 6dFGS are linked (69%), 1780 of 2281 galaxies in the *Spitzer* sample are linked (78%), and 293 of 391 SNIa hosts are linked (75%).

In order to ferret out bad data, we first look at consistency in distances between direct matches of alternate sources. There are 1524 galaxies with TF distances that are alternatively based on I -band photometry as reported in *Cosmicflows-2* or *Spitzer* [3.6] photometry introduced here. There were 17 strongly deviant cases (moduli differences > 0.8 mag). Nine of these are nearby galaxies with TRGB, Cepheid, SNIa, or SBF distances. Most of these galaxies are low luminosity, rather irregular systems poorly suited for the TF methodology. The nine *Spitzer* measures are rejected in favor of the other available distances.

In the other 8 cases the discordances are between the new *Spitzer* sample and the earlier I -band material. Aside from the sources of photometry, the only substantial differences are the assumed inclinations (recall Section 2.1). In all 8 cases, it is obvious from inspection of images that the new inclinations are more representative than the values used previously. The *Spitzer* distances are retained and the distances in *Cosmicflows-2* for these 8 galaxies are discarded. In the 1507 remaining matches, $\langle \mu_{spit} - \mu_{cf2} \rangle = -0.035 \pm 0.004$ with r.m.s. scatter of

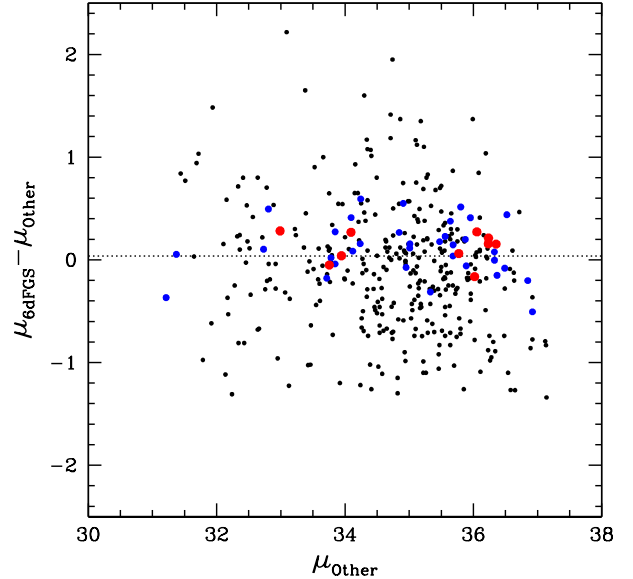


Figure 8. Comparison of 6dFGS type adjusted distance moduli with alternative measures. The 10 points in red represent nests with at least 10 distance measures by both 6dFGS and alternatives. The additional 34 points in blue represent nests with 4 – 9 distance measures by each. For cases represented by black points there are three or less measures by at least one of 6dFGS or other.

only ± 0.167 since usually only the photometry changes, and occasionally the inclinations.

There is a substantial incidence of SNIa in groups and multiple occurrences in the same nest afford a test of the dispersion in supernova distance measures. There are three SNIa in five nests and two such events in six nests in our sample. The estimated distance moduli for the 27 events can be compared jointly by calculating the r.m.s. dispersion from the mean distance moduli of their nests of residence. It is found that $\langle \mu_{nest_j}^{sn_i} - \bar{\mu}_{nest_j} \rangle = 0.02 \pm 0.21$ (10% scatter in distance) for 27 events. There is one strongly deviant case: sn2011ot in Abell 539, already noted in Section 5, differs from the group mean by 0.83 mag (4σ). The three supernovae in the cluster have a dispersion in modulus of 0.42 mag. Two supernovae ostensibly in Abell 1367, sn2006bd and sn2007ci, differ in distance modulus by 0.91, 52% in distance.

Figure 8 revisits the issue of the integration of the zero point for the 6dFGS FP distances with the other material. A comparison is made of distances to 381 Tully (2015b) nests. Averaging across all nests, with appropriate weights, there is a mean difference $\langle \mu_{6df} - \mu_{other} \rangle = \Delta\mu = 0.036 \pm 0.020$.

6.1. The Virgo Cluster

An important rung in the extragalactic distance ladder, the Virgo Cluster, presents an interesting example of insidious projection problems. There is always cause

to worry about group contamination, especially at low redshift where galaxies with similar velocities can be at different distances that are large in a relative sense. The Virgo Cluster is close, indeed, close enough that with the most accurate distance methodologies – Cepheids, TRGB, SNIa, SBF – foreground and background objects can be clearly distinguished. By misfortune there is a prominent Fornax-scale cluster, called Virgo W by [de Vaucouleurs \(1961\)](#), that lies at roughly twice the Virgo distance, positioned in projection such that the virial edges of the two clusters abut. The mean velocity of Virgo W is larger than for Virgo but the velocities within the dispersions of the two clusters completely overlap. Membership assignments with either of the two entities require good distances.

Although the main part of Virgo W projects outside the virial radius of the Virgo Cluster, there are known Virgo interlopers. The M Cloud ([Ftaclas et al. 1984](#)) lies at the background distance of Virgo W and projects fully onto the Virgo Cluster. Then there is the less substantial contaminant Virgo W' ([de Vaucouleurs 1961](#)) that lies 50% farther than Virgo and is fully within the Virgo spatial and velocity window.

This situation is discussed at greater length in the Virgo section on the paper on galaxy groups by [Tully \(2015a\)](#). The point was made that most of the known contamination lies within an area representing $\sim 40\%$ of the surface of Virgo. This perception had already informed the TF calibration analysis of [Tully & Pierce \(2000\)](#) and of subsequent studies ([Tully & Courtois 2012](#); [Sorce et al. 2013, 2014](#); [Neill et al. 2014](#)). Only galaxies lying in the $\sim 60\%$ of the cluster without much contamination were considered as TF calibrators. The same strategy was followed in this new study. There is the consequence that the new collection of distances provides information on many more galaxies in and around Virgo than are used in the calibration. It is of interest to examine what they tell us.

Figure 9 uses color to identify the projected locations of interloper galaxies imposed onto the Virgo Cluster. The circle with 6.8° radius is the projected second turnaround radius ([Tully 2015a](#)), a proxy for the virial radius. The main features in projection, Virgo W and W' and the M Cloud are identified with their second turnaround domains. Distances to the galaxies in colors and large symbols come from Cepheid measurements ([Freedman et al. 2001](#)) or from SBF observations ([Tomry et al. 2001](#); [Mei et al. 2007](#); [Blakeslee et al. 2009](#)). These galaxies lie either with Virgo W at twice the Virgo distance or half way between Virgo and Virgo W with Virgo W'. See the figure caption for details. So far, three foreground objects at ~ 9 Mpc have turned up from HST TRGB observations ([Karachentsev et al. 2014b](#)). The dotted lines in the figure show the bound-

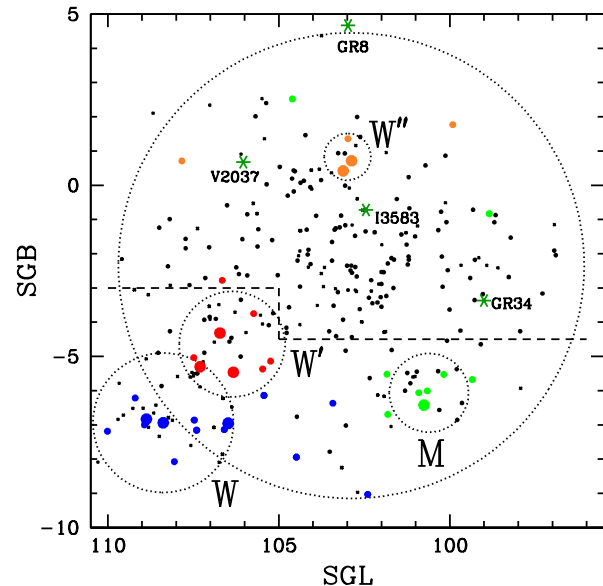


Figure 9. Known interloper galaxies with distances that distinguish them from Virgo Cluster members. Blue and green symbols identify galaxies in or related to the Virgo Cluster and M Cloud at twice the distance of the Virgo Cluster. Red and orange symbols identify galaxies associated with the Virgo W' Group midway between Virgo and Virgo W. Large symbols identify systems with distance measures more accurate than 10% while small symbols identify systems with distance measures with $\sim 20\%$ accuracy. The dark green stars locate dwarf galaxies to the foreground of the cluster. The black dots are at the positions of galaxies with 2MASS K magnitudes brighter than 11.75 lacking distance information. The second turnaround radii for the separate groups are indicated by dotted circles. The Virgo sample for the TF template is drawn exclusively from above the dashed lines.

ary isolating the domain of the Virgo TF calibrators – they all lie at positive SGB with respect to the boundary.

The uncertainties in distances from the TF and FP correlations do not allow for a clean rejection of contaminants. However, from Figure 10 the proposition of confusion is evident and, to a reasonable degree can be disentangled. Galaxies with local sheet velocities below 400 km s^{-1} are almost inevitably in the cluster, save for a few foreground dwarfs. Galaxies related to the background Virgo W have velocities greater than 1500 km s^{-1} and at 1.5 mag displacement are separable with distance information in all but pathological cases. The galaxies in and around Virgo W' are more problematic, with velocities near the Virgo mean and distance displacements of less than 2σ for FP and TF measures. However the Virgo W' feature is not populous.

It remains to compare distance results for the Virgo calibrator sample and the ensemble attributed to the cluster. The targets are seen in Figure 11. The calibrators are in red and others with distances from the

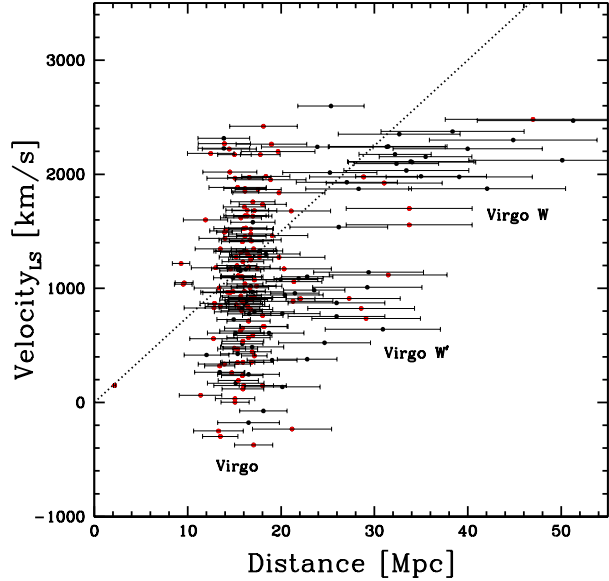


Figure 10. Distance vs. velocity for galaxies within a radius of 8° of the Virgo Cluster with distance estimates. Red/black: those with supergalactic latitude values above/below the dashed boundary in Fig. 9. Dotted line is Hubble law with $H_0 = 75$.

TF correlation attributed to the cluster, not the background, are in black. The mean modulus for the calibrator sample of 30 galaxies is 30.96 ± 0.11 with rms scatter 0.58. The mean modulus for the entire sample of 50 galaxies within the second turnaround radius is 31.04 ± 0.08 with rms scatter 0.53. Including 161 distance measures by all techniques that we use for the Virgo Cluster proper, the modulus is 31.01 (15.9 Mpc), with rms scatter 0.27 and nominal uncertainty 0.02 mag.

7. HOMOGENIZED ZERO POINT AND H_0

Our distance scale lattice involves three regimes. Nearby, within ~ 20 Mpc, our construction depends on Cepheid and TRGB distances, based on Pop I and Pop II foundations respectively and seen to agree. It is assumed for the Pop I scale that the Large Magellanic Cloud has a modulus 18.48 (Freedman et al. 2012). The Pop II scale is set by Horizontal Branch fits to M33, NGC 185, IC 1613, and Sculptor and Fornax dwarfs as described by Rizzi et al. (2007). Distances by both methods agree with the maser distance to NGC 4258 (Humphreys et al. 2013).

The SBF scale is tied directly to the Cepheid scale (Tonry et al. 2001; Blakeslee et al. 2009, 2010) and confirmed on average to be compatible with our other distances.

The TF and FP methods are operative in the broad regime 20 – 200 Mpc. The TF calibration is built through the 13 cluster slope template and the Cepheid-

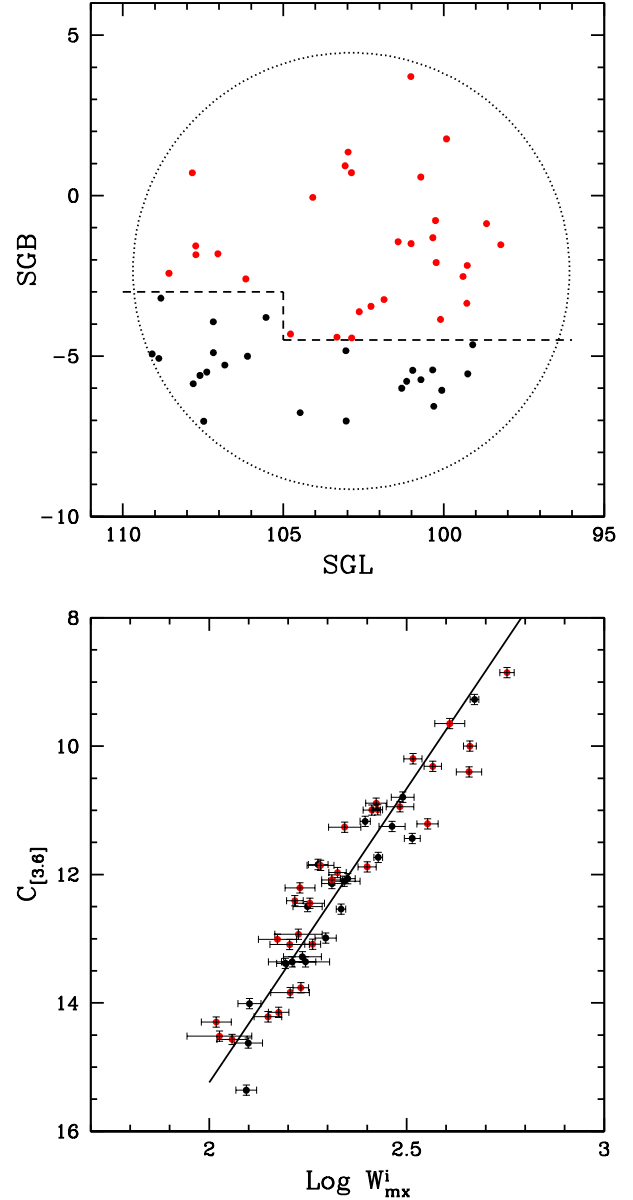


Figure 11. Galaxies associated with the Virgo Cluster with TF distances. Those in red, all above the dashed line in the top panel in the region relatively free of interloper contamination, contribute to the TF template calibration. Those in black are not used in the calibration. The combined samples contribute to the TF plot in the lower panel. The solid line has the 13 cluster template slope.

TRGB zero point constraints. There is a small difference in zero point between the scale established by the *Spitzer* sample and the earlier CF2 sample. The difference is evaluated in two ways. One way is to determine the difference in distance moduli $\Delta\mu = \mu_{spit} - \mu_{cf2}$ averaged over the 13 template calibrators. We find $\Delta\mu = -0.016$ with r.m.s. scatter ± 0.099 . Alternatively, the difference in distance moduli can be averaged over all 1507 galaxies in common, whence $\Delta\mu = -0.035$ with

scatter ± 0.167 . These offsets agree to within a half standard deviation. We accept a straight average of the two values, $\Delta\mu = -0.025$. The *Spitzer* recalibration results in distances 1.2% smaller on average.

The bulk of FP material in the CF2 compilation was restricted to clusters and the linkage of that sample was provided by cluster comparisons (Tully et al. 2013). The 6dGS FP distances were linked to the TF scale through clusters and individual galaxy matches. However, since the overlap of 6dFGS is limited, their contributions are excluded from the ladder to define H_0 .

SNIa, though sparse in coverage, are seen usefully at all relevant distances. The 309 SNIa available for *Cosmicflows-2* were given a compatible zero point. Now, as described in Section 5, 58 additional SNIa are added from Rest et al. (2014) with a statistically robust fit to the same zero point and 29 SNIa are added from Walker et al. (2015) with a less secure zero point fit. What is now required is a fit of the ensemble of SNIa to the new slightly revised calibration.

The comparison is enabled by the nests. As described in Section 6, 75% of SNIa hosts can be linked to the 2MASS nests of Tully (2015b). We then look for alternative distances for these nests within the *Spitzer* TF sample or the CF2 sample, excluding the SNIa contributions. With the large nests there can be multiple distance estimates by alternative methods and even occasions with multiple SNIa; there are five nests with three SNIa and six with two. Multiple measures can be averaged. Then in addition, there are six instances of SNIa hosts, not in established nests, but individually with an alternative distance estimate.

Comparisons are shown in Figure 12. SNIa moduli, on the CF2 scale, are plotted against the difference, $\mu_{sn} - \mu_{other}$, where μ_{other} can alternatively be from the *Spitzer* TF sample or the re-calibrated CF2 sample. The comparisons are in red if there are three or more alternative distances (over 100 in each of Virgo and Coma clusters and greater than 10 in 18 other cases), with the vertical error bars indicative of the number and quality of measures. Cases with one or two measures are black if from CF2 or green if from Spitzer. It is to be appreciated that the *Spitzer* and CF2 samples are not fully independent, since many of the SNIa, nests, and individual galaxies involved are the same.

Finally for the comparisons, the large blue symbols identify 9 cases where the SNIa host has a Cepheid distance. These cases plus the nest matches are averaged, taking due account of weights and the quasi-dependencies between *Spitzer* and CF2 samples, leading to the determination $\mu_{sn} - \mu_{other} = 0.021 \pm 0.023$, a statistical increase in distances of 1.0%. The offset from the earlier CF2 scale is only 1σ , but an adjustment of this observed amplitude is applied to the SNIa scale.

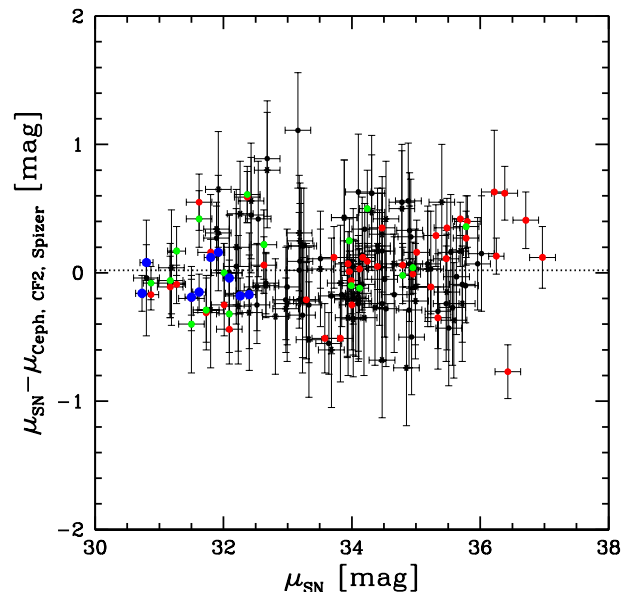


Figure 12. Fine-tuning of the SNIa zero point. SNIa distance moduli are given on the abscissa with the zero point established for the ensemble of SNIa in CF2. Differences between the SNIa distance moduli and distance moduli given by alternate methods are given on the ordinate axis on the CF2 scale. Large blue symbols: individual Cepheid–SNIa comparisons. Black and green symbols: comparisons involving 1 or 2 alternative distance measures against a SNIa measure in the same nest; black if from CF2 and green if from the new *Spitzer* compilation. Red symbols: comparisons involving 3 or more alternative measures (either from CF2 or *Spitzer*) against 1 to 3 SNIa measures within the same nest. The weighted average involving 9 individual Cepheid matches, 102 nests with CF2 measures, and 66 nests with *Spitzer* measures, implies SNIa moduli on the CF2 scale are high by 0.021 mag.

It must be noted that a fit solely to the 9 hosts of SNIa events with Cepheid distances gives $\mu_{sn} - \mu_{cephoid} = -0.059 \pm 0.047$. Accepting this scale would increase the SNIa scale by 0.080 in the modulus, an effect that would decrease H_0 by 3.8%. The 9 SNIa–Cepheid matches considered here strongly overlaps with the Riess et al. (2011) sample (we remove sn1981B and add sn1999by and sn2006X). It is seen in Fig. 12 that the direct SNIa–Cepheid comparisons are offset from the mean but not by a statistically significant amount. The Riess et al. article that focuses on a SNIa calibration with Cepheids alone is titled “A 3% Solution”. Precision cosmology is a fraught quest.

Returning to the Rest et al. (2014) compilation, this extensive sample extends beyond $z = 0.1$ to mid and high redshifts and, hence, can provide a bridge to the global Hubble Constant with minimal distortion from peculiar velocities. The component of the Rest et al. compilation of interest is a new sample of SNIa based on cadenced photometry with *Pan-STARRS* (Kaiser et al.

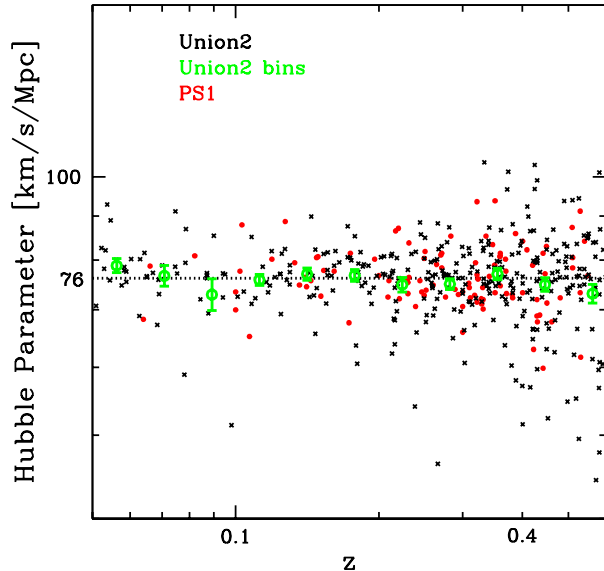


Figure 13. Fit to individual values of the Hubble parameters for supernovae in the *Union-2* (black crosses) and PS1 (red circles) samples in the interval $0.05 < z < 0.6$. Binned *Union-2* values are shown as open green circles. The logarithmically averaged value of $H_0 = 76.2 \text{ km s}^{-1} \text{ Mpc}^{-1}$ is shown by the dashed line.

2010). The Hubble Constant that is obtained with this new sample complements the parallel determination using the *Union-2* catalog of SNIa distances (Amanullah et al. 2010) that is the foundation for peculiar velocity estimates in *Cosmicflows-2* (Sorice et al. 2012b; Neill et al. 2014).

Figure 13 shows the dependence of the Hubble parameter, H_i , as a function of redshift for the two alternative SNIa samples, *Union-2* and *Pan-STARRS* (PS1). The parameter H_i has the cosmological corrections of Eq. 5, assuming $\Omega_m = 0.27$ and a flat cosmic topology. Separately, the *Union-2* sample is consistent with $H_0 = 75.9 \text{ km s}^{-1} \text{ Mpc}^{-1}$ and the PS1 sample implies $H_0 = 76.4 \text{ km s}^{-1} \text{ Mpc}^{-1}$. We take an average and accept $H_0 = 76.2 \text{ km s}^{-1} \text{ Mpc}^{-1}$. There is a mild dependence on the cosmological density parameter, with H_0 increased/decreased one unit if Ω_m is decreased/increased 0.04.

There are both random and systematic uncertainties in the estimate of H_0 . The largest random uncertainty (± 0.079 in the modulus) lies with the zero point calibration to the TF relation based on 33 galaxies with Cepheid or TRGB distances. The SNIa zero point is directly established through 9 Cepheid distances and less directly established through over 100 group affiliations and has an uncertainty of ± 0.046 . Then there is an uncertainty of ± 0.030 for the fit to the mean Hubble parameter in Figure 13. Added in quadrature, the ran-

dom error is ± 0.096 , 4.5% in distance and affect on H_0 . Systematic effects are harder to quantify, but the components of concern and estimates of uncertainties are the Cepheid and TRGB zero points (± 0.05), possible variations in SNIa properties that manifest in distance (Rigault et al. 2015) (± 0.05), and uncertainties in the cosmological model corrections (± 0.027). Systematics crudely add in quadrature to 0.076, 3.5% in distance and H_0 .

8. THE CATALOG

Information is gathered on two levels. At level one are individual galaxies. In cases with multiple distance measurements, averaged moduli are determined with weights appropriate to the different inputs. At level two are groups, specifically the nests of Tully (2015b) which supplies group averaged positions and velocities plus summed K band luminosities and estimated masses. Group distance moduli are derived by weighted averaging of all the moduli available for group members.

The group catalog (Tully 2015b) was built exclusively from 2MRS, the 2MASS $K < 11.75$ redshift sample (Huchra et al. 2012). The catalog includes "nests" as small as only one member. *Cosmicflows-3* contains entries that are not in 2MRS. It was described in Section 6 that roughly three-quarters of *Cosmicflows-3* galaxies are assigned to a 2MRS nest. Galaxies that define the distance to a nest and galaxies that define the other properties (position, velocity, luminosity) need not be identical. Then additionally, there are galaxies with distances that have no nest assignment. These cases are taken to be singles.

The catalog is presented as two tables, abbreviated in this text but available on-line in complete form. Table 3 gives summary group information for 11,508 nests, 1704 with two or more distances and 9804 singles. The Virgo Cluster (nest 100002) has the most galaxies with measured distances with 161. There are 125 groups with 10 or more galaxies with distances. Table 4 couples the individual and group information. In this table, a row is dedicated to each of the 17,669 galaxies with distance measurements. The first 41 columns provide information on the specific galaxy, including distances from alternative sources. Then the last 30 columns give information on the associated nest, drawn from Table 3. The material in these latter columns is the same for every member of a given nest.

The distance moduli, both for individual galaxies and again for groups, are weighted averages with individual weights $w_i = 1/\epsilon_i^2$ where the uncertainty in a modulus is ϵ_i , giving total weights $w_t = \sum_i^N w_i$, and error on the averaged modulus $\epsilon_\mu = 1/w_t^{1/2}$. For groups with many distance measures this formal error is as small as 0.02 mag, 3 times smaller than reasonable expectations of

systematic errors.

Description of Tables 3 and 4. In the case of the group catalog, Table 3, columns 1–30 are mimicked in columns 42–71 of Table 4, the catalog of individual sources. The following is a description of the columns in Table 4. This table is also available, with updates, at the *Extragalactic Distance Database*.¹

1. PGC: Principal Galaxies Catalog ID (Makarov et al. 2014)
2. d : Luminosity distance measurement for individual galaxy. Weighted average of the distance moduli if more than one source. [Mpc]
3. N_d : Numbers of sources of distance measures for the individual galaxy.
4. $\langle \mu \rangle$: Luminosity distance modulus measurement for individual galaxy. Weighted average if more than one source. [mag]
5. ϵ_μ : One standard deviation uncertainty in distance modulus. Caution: Different from CF2 entry where the fractional error in distance is quoted. [mag]
6. C: indicates the availability of a Cepheid measurement.
7. T: indicates the availability of a Tip of the Red Giant Branch measurement from an HST observation and reduced in a standard way (Jacobs et al. 2009).
8. L: indicates the availability of a Tip of the Red Giant Branch measurement extracted from the literature.
9. M: indicates the availability of a high quality miscellaneous measurement (RR Lyrae, Horizontal Branch, Eclipsing Binary, Maser).
10. S: indicates the availability of a Surface Brightness Fluctuation measurement.
11. N: indicates the availability of a Type Ia Supernova measurement in the host galaxy.
12. H: indicates the availability of a TF relation measurement based on optical photometry, as reported in CF2.
13. I: indicates the availability of a TF relation measurement based on photometry at $3.6 \mu\text{m}$ with *Spitzer Space Telescope*.
14. F: indicates the availability of a Fundamental Plane measurement from the ENEAR, EFAR, or SMAC experiments as reported in CF2.
15. P: indicates a Fundamental Plane measurement from 6dFGS (Springob et al. 2014).
16. μ_{cf2} : Distance modulus carried over from *Cosmicflows-2*. [mag]
17. ϵ_μ^{cf2} : One standard deviation uncertainty in distance modulus carried over from CF2. [mag]
18. SN: Supernova identification.
19. N_{sn} : Number of separate analyses of the supernova.
20. μ_{sn} : Luminosity distance modulus of supernova averaged over all contributions. [mag]
21. μ_{spit} : Luminosity distance modulus determined from the TF correlation using *Spitzer* [3.6] band photometry. [mag]
22. ϵ_μ^{spit} : One standard deviation uncertainty in distance modulus determined from TF relation using *Spitzer* [3.6] photometry. Uncertainty 0.45 if from color corrected relation; 0.54 if color information lacking. [mag]
23. μ_{6df} : Luminosity distance modulus from 6dFGS (Springob et al. 2014) Fundamental Plane with *Cosmicflows-3* zero point. [mag]
24. ϵ_μ^{6df} : One standard deviation uncertainty in distance modulus determined from 6dFGS Fundamental Plane. [mag]
25. M_t : 6dFGS morphology type code (Campbell+ 2015).
26. RAJ : Right ascension, epoch 2000. [hhmmss.s]
27. $DecJ$: Declination, epoch 2000. [ddmmss]
28. Gl_{on} : Galactic longitude. [deg]
29. Gl_{at} : Galactic latitude. [deg]
30. SGL : Supergalactic longitude. [deg]
31. SGB : Supergalactic latitude. [deg]
32. Ty : Morphological type; RC3 numeric code (Makarov et al. 2014).
33. A_{sf} : Reddening at B band (Schlafly & Finkbeiner 2011). [mag]
34. B_t : Total B magnitude from LEDA. [mag]

¹ <http://edd.ifa.hawaii.edu>

35. K_s : 2MASS K_s magnitude with corrections from [Lavaux & Hudson \(2011\)](#). [mag]
36. V_h : Heliocentric velocity. [km s^{-1}]
37. V_{gsr} : Velocity in Galactic standard of rest; circular velocity at Sun of 239 km s^{-1} ; total velocity 251 km s^{-1} toward $\ell = 90$, $b = 0$ ([van der Marel et al. 2012](#)). [km s^{-1}]
38. V_{LS} : Velocity in Local Sheet standard of rest ([Tully et al. 2008](#)). [km s^{-1}]
39. V_{cmb} : Velocity in CMB standard of rest ([Fixsen et al. 1996](#)). [km s^{-1}]
40. V_{mod} : Velocity in CMB standard of rest adjusted in accordance with a cosmological model with $\Omega_{matter} = 0.27$ and $\Omega_{\Lambda} = 0.73$. [km s^{-1}]
41. Name: Common name.
42. Nest: 2MASS "nest" group identification ([Tully 2015b](#)).
43. N_d^{gp} : Number of galaxies in group with distance measures.
44. $\langle \mu \rangle^{gp}$: Luminosity distance modulus to group; weighted over all contributions. [mag]
45. ϵ_{μ}^{gp} : One standard deviation uncertainty in group distance modulus. [mag]
46. d^{gp} : Luminosity distance to group; weighted average of distance moduli. [Mpc]
47. Abell: Abell Cluster identification; ASxxx are from the southern supplement list.
48. Group Name: Alternative name for group or cluster.
49. N_v : Number of galaxies in group with positions and velocities in the 2MRS catalog ([Huchra et al. 2012](#)).
50. PGC1: Principal Galaxies Catalog ID of brightest group member.
51. Gl_{on}^{gp} : Galactic longitude of group. [deg]
52. Gl_{at}^{gp} : Galactic latitude of group. [deg]
53. SGL^{gp} : Supergalactic longitude of group; luminosity weighted (2MASS K_s). [deg]
54. SGB^{gp} : Supergalactic latitude of group; luminosity weighted (2MASS K_s). [deg]
55. $LogL^{gp}$: Log summed K_s luminosity of group; adjusted by correction factor for lost light ([Tully 2015b](#)). Assumed distance given by group velocity V_{mod}^{gp} and $H_0 = 75$. [$\log L_{\odot}^K$]
56. cf : Luminosity selection function correction factor.
57. σ_p : Projected velocity dispersion anticipated by corrected intrinsic luminosity ([Tully 2015a](#)). [km s^{-1}]
58. R_{2t} : Projected second turnaround radius anticipated by corrected intrinsic luminosity ([Tully 2015a](#)). Assumed distance given by group velocity V_{mod}^{gp} and $H_0 = 75$. [Mpc]
59. V_h^{gp} : Group heliocentric velocity. [km s^{-1}]
60. V_{gsr}^{gp} : Group velocity in Galactic standard of rest; circular velocity at Sun of 239 km s^{-1} ; total velocity 251 km s^{-1} toward $\ell = 90$, $b = 0$ ([van der Marel et al. 2012](#)). [km s^{-1}]
61. V_{LS}^{gp} : Group velocity in Local Sheet standard of rest ([Tully et al. 2008](#)). [km s^{-1}]
62. V_{cmb}^{gp} : Group velocity in CMB standard of rest ([Fixsen et al. 1996](#)). [km s^{-1}]
63. V_{mod}^{gp} : Group velocity in CMB standard of rest adjusted in accordance with a cosmological model with $\Omega_{matter} = 0.27$ and $\Omega_{\Lambda} = 0.73$. [km s^{-1}]
64. V_{rms} : Group velocity dispersion. [km s^{-1}]
65. M_{12}^{bw} : Group mass in units of $10^{12} M_{\odot}$ from virial theorem with bi-weight dispersion and radius parameters ([Tully 2015b](#)). Assumed distance given by group velocity V_{mod}^{gp} and $H_0 = 75$. [$10^{12} M_{\odot}$]
66. M_{12}^L : Group mass in units of $10^{12} M_{\odot}$ based on corrected luminosity and M/L prescription ([Tully 2015b](#)). Assumed distance given by group velocity V_{mod}^{gp} and $H_0 = 75$. [$10^{12} M_{\odot}$]
67. LDC: Low density group ID ([Crook et al. 2007](#)).
68. HDC: High density group ID ([Crook et al. 2007](#)).
69. 2M++: Group ID from 2MASS++ catalog ([Lavaux & Hudson 2011](#)).
70. M&K: Group ID from catalog by ([Makarov & Karachentsev 2011](#)).
71. Icnt: Internal reference ID.

9. DISCUSSION

The sky coverage is heterogeneous as evident in Figures 14 – 16, which show the projected distribution of the 17,669 galaxies in *Cosmicflows-3* on three different scales. Figure 14 captures essentially the full domain of the catalog, in the ensemble in the upper left panel and by components in the other panels. The numerical improvement of CF3 over CF2 is directly seen by the difference between the top left and right panels. The two major new components are shown separately in the bottom panels. Figure 15 is a zoom to the inner regions of these same panels. Figure 16 is a further zoom of the previous lower right panels showing the *Spitzer* TF sample (green) and adds the TRGB and Cepheid contributions (blue) and SNIa (red).

The most evident feature of the maps is the tremendous numeric contribution of the 6dFGS sample, in orange in the left panels of Figures 14 and 15. Where there had been a deficiency of information in the celestial south in CF2, now the coverage is dense in that sector. The distribution of the 6dFGS sample (Springob et al. 2014) in velocity is seen in the orange histogram of Figure 17. This sample dominates the global histogram in the range 8,000 – 16,000 km s⁻¹.

The *Spitzer* TF sample is more local. It is to be recalled that there are three dominant programmatic contributions. The galaxies from *S⁴G* (Sheth et al. 2010) are constrained to 40 Mpc (~ 3000 km s⁻¹) and $|b| > 30^\circ$. Our *Cosmic Flows with Spitzer* program (Sorce et al. 2014) complemented *S⁴G* by extending to low Galactic latitudes, pushing into the wedges of incompleteness evident in Figures 14 – 16. Then this latter program used its remaining available observing time on extreme edge-on disk systems at 3,000 – 10,000 km s⁻¹.

The SNIa sample has grown incrementally from CF2. Although the numbers are modest (391), the events are dispersed, they explore larger distances, and each contribution has a weight 4 – 7 times greater than a TF or FP measure. The combined Cepheid and TRGB sample has also grown incrementally. The associated galaxies are nearby, as seen in Figure 16. Our understanding of the kinematics of the region within 10 Mpc is now very good (Karachentsev et al. 2015b).

Figure 18 is a variant of Figures 14 – 16. Here, nests are shown with increasing resolution from the top panel to the bottom. The symbol colors and sizes distinguish nests by distance uncertainty, strongly correlated with the number of measures. The information is richest nearby, as would be expected.

Cosmicflows-3 is by far the largest collection of distances at this time. It will be exciting to translate the distances into deviations from cosmic expansion and develop compatible models of the distribution of matter.

The radial component of a deviation from cosmic expansion, the so-called peculiar velocity is

$$V_{pec} = (V_{mod} - H_0d)/(1 + H_0d/c) \quad (8)$$

where V_{mod} is the velocity of a galaxy with cosmological modifications as defined in Eq. 5 (Davis & Scrimgeour 2014). As is well known, though, peculiar velocity uncertainties grow with distance and become larger than physical peculiar velocities for individual measurements already at systemic velocities of 2,000–3,000 km s⁻¹ depending on the methodology. Averaging within groups helps considerably. Still, further smoothing is inevitably necessary. Fortunately the task is not hopeless because of large scale coherence in galaxy motions.

Springob et al. (2014) alert us to directionally dependent departures between the velocity field inferred from 6dFGS distances and the velocity fields derived from two independent redshift surveys (Branchini et al. 1999; Erdođdu et al. 2006). Their peculiar velocities are more positive than anticipated from models derived from the redshift surveys in the direction toward the Shapley concentration and more negative than anticipated toward the Pisces-Cetus supercluster (Tully et al. 1992). The implications of these concerns will be evaluated with detailed modeling in later studies.

Another issue of concern is the reliability of our determination of the Hubble Constant of 76.2 km s⁻¹ Mpc⁻¹. This value is slightly higher than we determined recently of 74.4 (Neill et al. 2014) and 75.2 (Sorce et al. 2014). The increase here results from the addition of 26 galaxies to the 13 cluster TF template, minor cluster membership revisions, and some improved inclinations. The changes are slight but remind us of sensitivity to systematics.

We determine H_0 from a zero point calibration of SNIa and then application to two samples of SNIa at $0.05 < z < 0.6$, a range that should not be affected by peculiar velocities nor is strongly dependent on choice of cosmology. The zero point is anchored by Cepheid and TRGB distances and bootstraps through distances to clusters set by SBF, TF, and the FP programs ENEAR, EFAR, and SMAC. The 6dFGS material is not used because of limited sample overlap. An alternative strategy is to jump directly to a SNIa calibration using the few SNIa host galaxies with Cepheid distances (Riess et al. 2011). It is seen in Figure 12 that these contributions to our calibration lie slightly below the mean. A calibration based only on these galaxies with Cepheid distances gives a value of H_0 3.8% lower of 73.4, consistent with Riess et al. Estimates of systematics should encompass this difference.

Cosmicflows-3 does not directly provide peculiar velocities. Errors that are Gaussian distributed in distance modulus are lognormal in distance and pe-

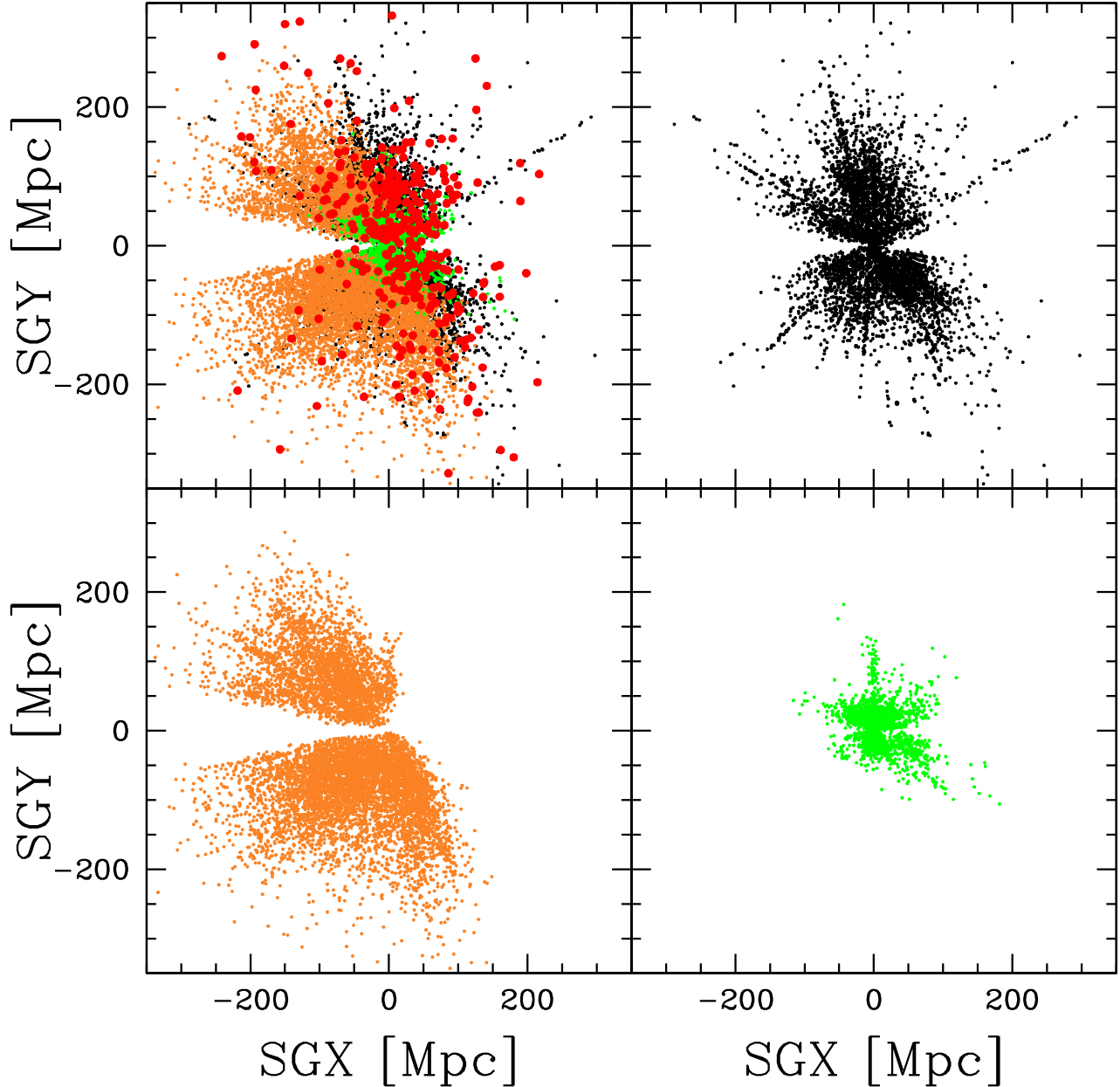


Figure 14. Projection of individual CF3 distances into supergalactic SGX vs. SGY. Upper left: all galaxies; the earlier CF2 sample is represented in black, the 6dFGS contribution is orange, the *Spitzer* TF sample is green, and SNIa hosts are shown in red. Upper right: only the earlier CF2 sample. Lower left: only the 6dFGS sample. Lower right: only the *Spitzer* TF sample.

cular velocities, skewing peculiar velocity measurements to negative values. There are interesting approaches to address this problem (Nusser & Davis 1995; Watkins & Feldman 2015). The great concern is a form of Malmquist bias (Lynden-Bell 1992; Strauss & Willick 1995). If peculiar velocities are evaluated at the sites of measured distances there will be artificial flows. Galaxies will have scattered from the places of physical origin that are most represented and tend to have erroneous peculiar velocity components that point back to their true

positions. This generic description applies to both the so-called homogeneous and inhomogeneous Malmquist biases. Biases are much reduced by evaluating distance measures at the sites of systematic velocities since observed velocities have small errors.

We adopt the stance that distances and peculiar velocities should not be confounded. The effort in this work is to provide distances that have uncertainties but are individually unbiased. We may not be fully successful, with so much dependence on literature sources and as

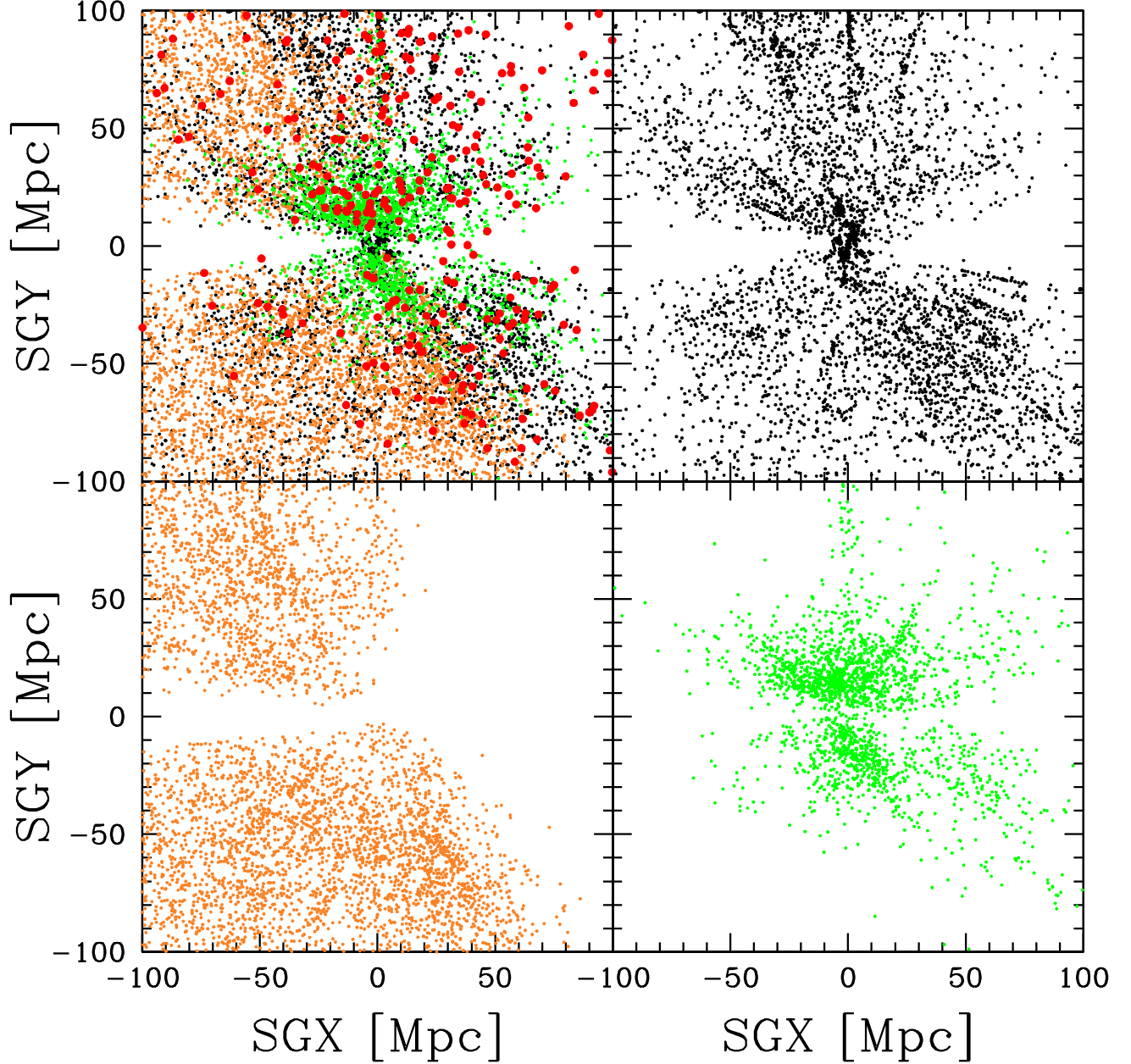


Figure 15. Zoom of Fig. 14.

yet insufficient overlaps in some instances. In any event, what is provided are distances in Mpc, independent of velocities. Velocities are provided too, and together with distances one can infer a Hubble Constant, modulo flows and systematics.

A first-look visual impression of the peculiar velocity field is given in Figure 19 with two scales. Objects within $\pm 3,000 \text{ km s}^{-1}$ of the supergalactic equator drawn from the groups catalog are plotted at positions given by velocities in the CMB frame with colors indicative of peculiar velocities. The peculiar velocities repre-

sented in the plots are calculated using the formulation by [Watkins & Feldman \(2015\)](#) that are statistically unbiased and have Gaussian distributed errors:

$$V_{pec}^{wf} = \frac{V_{mod}}{1 + V_{mod}/c} \log(V_{mod}/H_0 d). \quad (9)$$

This description of peculiar velocities breaks down nearby where real peculiar velocities are substantial compared with the estimator. We invoke a ramp within $V_{LS} = 3,000 \text{ km s}^{-1}$, linearly transitioning from V_{pec} given by Eq. 8 to V_{pec}^{wf} given by Eq. 9 as V_{LS} runs from zero to $3,000 \text{ km s}^{-1}$.

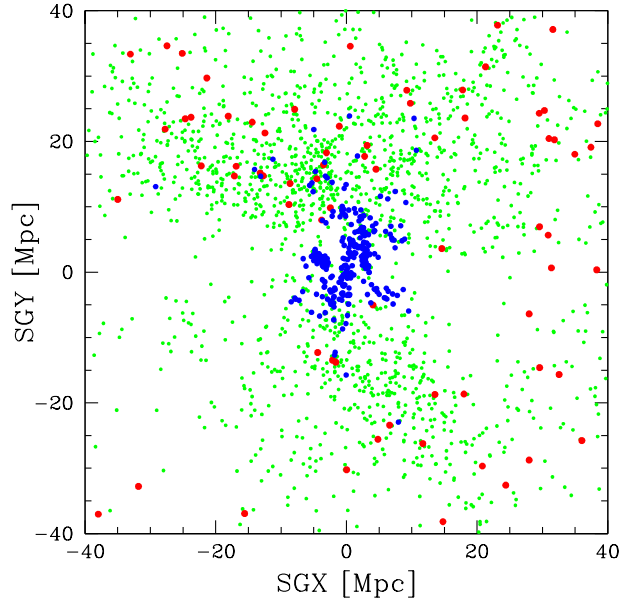


Figure 16. Further zoom of lower right panel of Figs. 14 and 15 with the inclusion of SNIa hosts in red and contributions from Cepheid and TRGB measurements in blue.

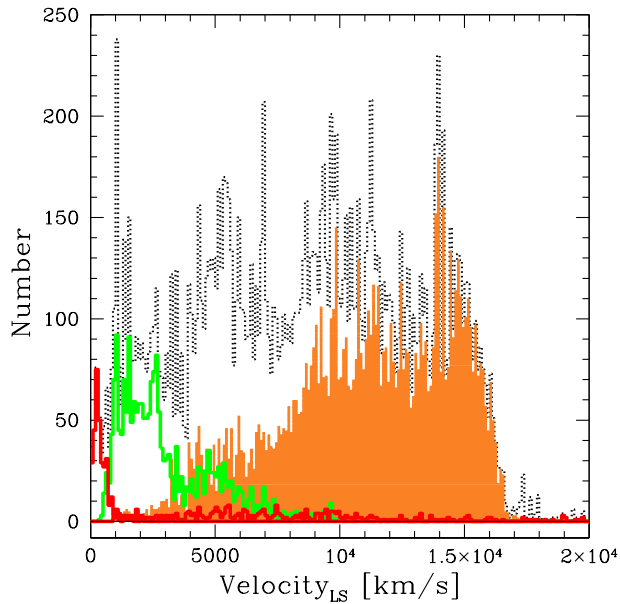


Figure 17. Velocity distribution of the sample. The distribution for all galaxies in CF3 is given by the black dashed histogram. The 6dFGS component is shown in orange and the *Spitzer* TF sample is in green. The red histogram combines the TRGB and Cepheid contributions (the peak at low velocities) and SNIa (strung out over a wide range of velocities). Velocities are group averaged values to minimize the effects of velocity dispersions in groups.

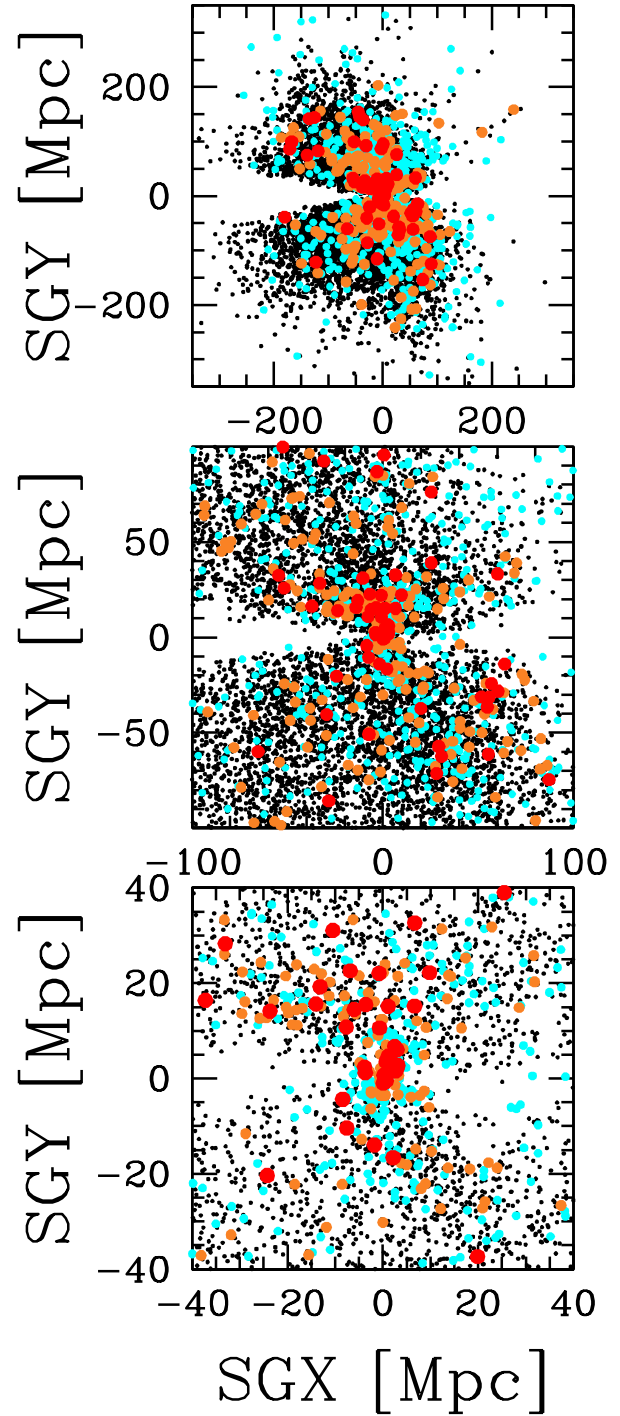


Figure 18. Projection of grouped CF3 distances into supergalactic SGX vs. SGY. Groups with $e_{\mu}^{gp} \leq 0.10$ are in red, with $0.10 < e_{\mu}^{gp} \leq 0.16$ are in orange, with $0.16 < e_{\mu}^{gp} \leq 0.25$ are in cyan, and with $e_{\mu}^{gp} > 0.25$ are black. The three panels illustrate three different scales.

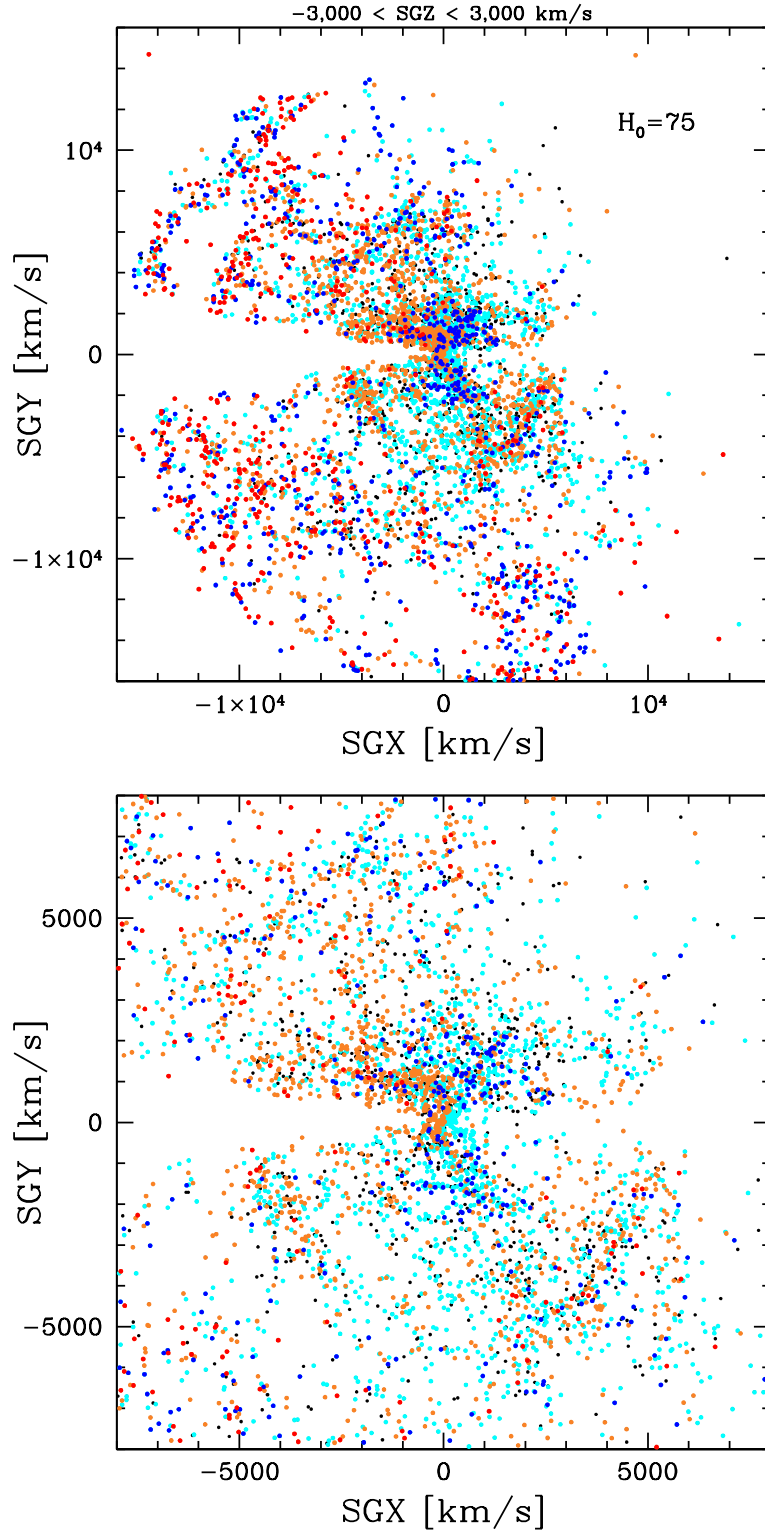


Figure 19. Peculiar velocities within $\pm 3000 \text{ km s}^{-1}$ of the supergalactic equator. $V_{pec}^{wf} > 100 \text{ km s}^{-1}$ orange, $> 800 \text{ km s}^{-1}$ red. $V_{pec}^{wf} < -100 \text{ km s}^{-1}$ cyan, $< -800 \text{ km s}^{-1}$ blue. Lower panel is a blow-up of the central region. $H_0 = 75 \text{ km s}^{-1} \text{ Mpc}^{-1}$ assumed.

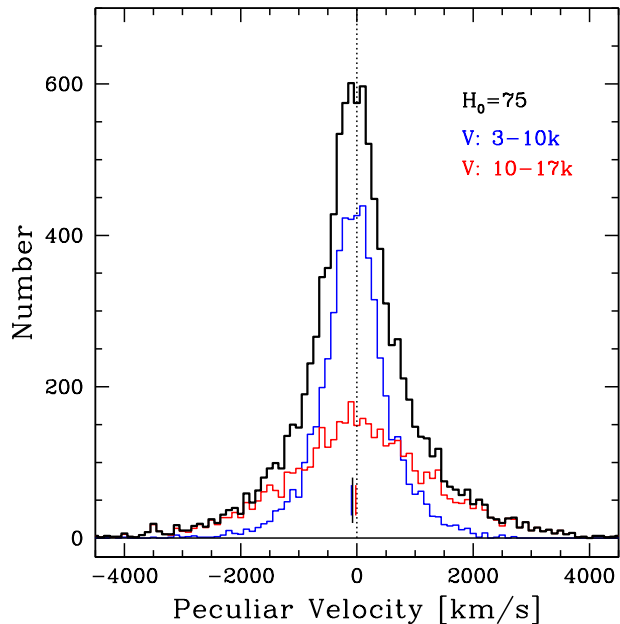


Figure 20. Histogram of peculiar velocities, assuming $H_0 = 75 \text{ km s}^{-1} \text{ Mpc}^{-1}$. The black histogram represents the entire sample. The blue histogram is built from galaxies with velocities between 3,000 and 10,000 km s^{-1} and the red histogram, from galaxies outside 10,000 km s^{-1} .

The most evident feature of Figure 19 is the prominence of blue shades at positive SGX, negative SGY and red shades at negative SGX, positive SGY. This trend is a manifestation of the well known flow (Lynden-Bell et al. 1988) toward the so-called Great Attractor. There is great interest in the amplitude and extent of bulk flows (Feldman et al. 2010; Nusser & Davis 2011; Hoffman et al. 2015). Any comment on higher order structure is beyond the scope of this paper. However we should dwell on the peculiar velocity monopole term: overall expansion or contraction with no preferred direction. It is seen that there is dependence on H_0 with either of Eqs. 8 or 9. As the accepted value of H_0 is increased, peculiar velocities become more negative, so with a very large H_0 there is a general infall of galaxies. By contrast, as the choice of H_0 is decreased, peculiar velocities become more positive, tending toward outflow. The display seen in Figure 19 is based on the choice $H_0 = 75 \text{ km s}^{-1} \text{ Mpc}^{-1}$. The justification for the choice is given with Figures 20 and 21. The first of these two figures presents histograms of V_{pec}^{wf} assuming $H_0 = 75$, with separation between galaxies within and beyond 10,000 km s^{-1} given by the colored histograms and the ensemble in black. The vertical bars near the origin mark the median values of the three histograms (-77 , -96 , and -20 km s^{-1} for the ensemble, inner, and outer samples, respectively).

Figure 21 deserves particular attention regarding the

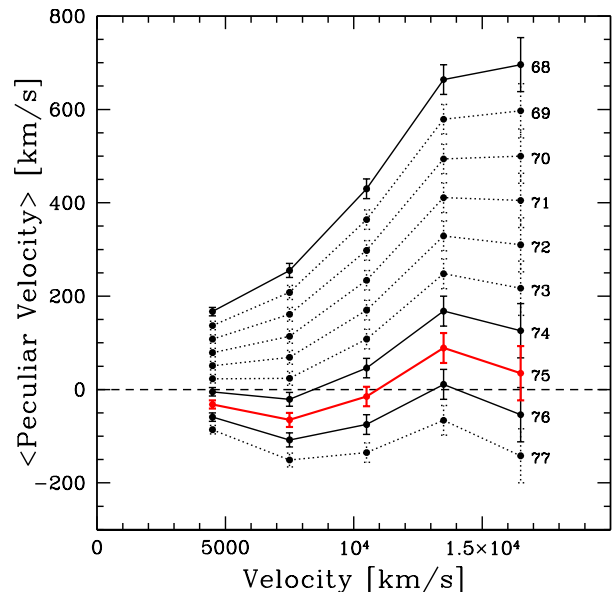


Figure 21. Dependence of peculiar velocities on choice of H_0 . Mean peculiar velocities and standard deviations are given in systemic velocity bins for choices of H_0 between 68 and 77 $\text{km s}^{-1} \text{ Mpc}^{-1}$.

choice of H_0 . The points with error bars give mean values for peculiar velocities in systemic velocity bins (ignoring $V_{LS} < 3000 \text{ km s}^{-1}$ where local effects dominated). Dotted and solid lines link bins associated with the same values of H_0 . Below the dashed line at zero peculiar velocity is the domain of monopole infall and above the dashed line is the domain of outflow. A characteristic of a poor choice of H_0 would be a monotonic increase in mean peculiar velocities with increasing systemic velocity if H_0 is taken too low and the inverse if H_0 is taken too high. From these considerations, a value of $H_0 \sim 75 \text{ km s}^{-1} \text{ Mpc}^{-1}$ is preferred. The trends in peculiar velocity with systemic velocity only flatten out around $H_0 \sim 76.5$, but there would be a generalized infall of $\sim -80 \text{ km s}^{-1}$ in that case. The choice $H_0 = 75$, shown in red, minimizes the monopole term with the ensemble of the *Cosmicflows-3* distances. With this choice, there is a net tiny infall within 10,000 km s^{-1} and a net tiny outflow beyond 10,000 km s^{-1} .

We are unable to know if this minimization of the monopole describes the true situation. If the true value of H_0 is 76.2 as indicated by the SNIa calibration then there would be an overall inflow within the region of study. The implication would be that the local region is over dense which would be a disputed conclusion. Alternatively, the value of $H_0 = 68$ from studies of CMB fluctuations (Planck Collaboration et al. 2015) can be entertained. The dramatic implication seen in Figure 21 would be a massive outflow reaching 700 km s^{-1} by 0.05c. The situation with such a low value of H_0 is

unrealistic. The displacement of the median peculiar velocity for the ensemble is $+40 \text{ km s}^{-1}$ as H_0 is decreased one unit. A tolerance of $\pm 100 \text{ km s}^{-1}$ on the monopole averaged over all velocities $< 16,000 \text{ km s}^{-1}$ translates to a restriction on H_0 to 75 ± 2 . We can only reconcile with the Planck Collaboration result if there is an unexpectedly large error in the zero point calibration of our distances. Views on uncertainties in the initial steps of the distance ladder have been expressed by Efstathiou (2014) and, as this paper goes to press, by Riess et al. (2016).

10. SUMMARY

Distances are assembled for 17,669 galaxies; 7,865 in 1,704 nests with two or more measures and 9,804 singles. *Cosmicflows-3* extends the previous catalog with two major new contributions: our 2,257 distances based on the TF method using [3.6] band *Spitzer Space Telescope* photometry (Sorce et al. 2014) and 8,885 literature distances based on the FP method from the 6dFGS collaboration (Campbell et al. 2014; Springob et al. 2014). There are also two incremental extensions: a 29% increase in the number of TRGB distances arising from our ongoing *Hubble Space Telescope* program (Jacobs et al. 2009) and a 27% increase in the number of SNIa distances extracted from the literature (Rest et al. 2014; Walker et al. 2015).

The implementation of a new group catalog (Tully 2015b) is an important supplement. Group (nest) positions and velocities are averaged across known members and distances are averaged across those members with distance estimates.

A global value of the Hubble Constant of 76.2 ± 3.4 (rand.) ± 2.7 (sys.) $\text{km s}^{-1} \text{ Mpc}^{-1}$ is determined by establishing the SNIa zero point with 168 comparisons of distances to nests and nine direct Cepheid comparisons and then using that calibration to establish H_0 at $0.05 < z < 0.6$ averaging two SNIa samples (Amanullah et al.

2010; Rest et al. 2014). An alternate estimate of the Hubble Constant is provided by the minimization of the monopole term in the ensemble of peculiar velocities. If global infall or outflow is assumed to be less than 100 km s^{-1} then $H_0 = 75 \pm 2 \text{ km s}^{-1}$.

There are as yet few cross-checks with the important 6dFGS component of the collection. Hopefully the situation will improve with the fourth release of *Cosmicflows*, anticipated to include a large all-sky sample of TF distances using $3.4\mu\text{m}$ and $4.5\mu\text{m}$ photometry from WISE, the *Wide-field Infrared Satellite Explorer*. In the meantime, in addition to the on-line resources provided by this journal, *Cosmicflows-3* and updates can be accessed at <http://edd.ifa.hawaii.edu>.

Note added in proof: Replacing the Cepheid – SNIa comparisons in Fig. 12 with values given in Riess et al. (2016) reduces the H_0 calibration illustrated in Fig. 13 from 76.2 to 75.5 $\text{km s}^{-1} \text{ Mpc}^{-1}$.

Acknowledgements

Many people have contributed directly or indirectly to this substantial undertaking. Special thanks to Igor Karachentsev, Dmitry Makarov, Don Neill, Luca Rizzi, Mark Seibert, Ed Shaya, Kartik Sheth, and Po-Feng Wu. It is hard to imagine how this catalog could have been assembled without the resources of NED, the *NASA/IPAC Extragalactic Database*, and the Lyon extragalactic database *HyperLeda*. Financial support for the *Cosmicflows* program has been provided by the US National Science Foundation award AST09-08846, an award from the Jet Propulsion Lab for observations with *Spitzer Space Telescope*, and NASA award NNX12AE70G for analysis of data from the *Wide-field Infrared Survey Explorer*. Additional support has been provided by the Lyon Institute of Origins under grant ANR-10-LABX-66 and the CNRS under PICS-06233.

REFERENCES

- Amanullah, R., Lidman, C., Rubin, D., et al. 2010, *ApJ*, 716, 712
 Blakeslee, J. P., Jordán, A., Mei, S., et al. 2009, *ApJ*, 694, 556
 Blakeslee, J. P., Cantiello, M., Mei, S., et al. 2010, *ApJ*, 724, 657
 Branchini, E., Teodoro, L., Frenk, C. S., et al. 1999, *MNRAS*, 308, 1
 Campbell, L. A., Lucey, J. R., Colless, M., et al. 2014, *MNRAS*, 443, 1231
 Cortese, L., Fogarty, L. M. R., Ho, I.-T., et al. 2014, *ApJL*, 795, L37
 Courtois, H. M., Tully, R. B., Fisher, J. R., et al. 2009, *AJ*, 138, 1938
 Courtois, H. M., Tully, R. B., Makarov, D. I., et al. 2011, *MNRAS*, 414, 2005
 Crook, A. C., Huchra, J. P., Martimbeau, N., et al. 2007, *ApJ*, 655, 790
 Dalcanton, J. J., Williams, B. F., Melbourne, J. L., et al. 2012, *ApJS*, 198, 6
 Davis, T. M., & Scrimgeour, M. I. 2014, *MNRAS*, 442, 1117
 de Grijs, R., Wicker, J. E., & Bono, G. 2014, *AJ*, 147, 122
 de Vaucouleurs, G. 1961, *ApJS*, 6, 213
 Djorgovski, S., & Davis, M. 1987, *ApJ*, 313, 59
 Dressler, A., Lynden-Bell, D., Burstein, D., et al. 1987, *ApJ*, 313, 42
 Efstathiou, G. 2014, *MNRAS*, 440, 1138
 Erdođdu, P., Lahav, O., Huchra, J. P., et al. 2006, *MNRAS*, 373, 45
 Feldman, H. A., Watkins, R., & Hudson, M. J. 2010, *MNRAS*, 407, 2328
 Fixsen, D. J., Cheng, E. S., Gales, J. M., et al. 1996, *ApJ*, 473, 576

- Folatelli, G., Phillips, M. M., Burns, C. R., et al. 2010, *AJ*, 139, 120
- Freedman, W. L., Madore, B. F., Scowcroft, V., et al. 2012, *ApJ*, 758, 24
- Freedman, W. L., Madore, B. F., Gibson, B. K., et al. 2001, *ApJ*, 553, 47
- Ftaclas, C., Struble, M. F., & Fanelli, M. N. 1984, *ApJ*, 282, 19
- Giovanelli, R., Haynes, M. P., Herter, T., et al. 1997, *AJ*, 113, 22
- Hoffman, Y., Courtois, H. M., & Tully, R. B. 2015, *MNRAS*, 449, 4494
- Huchra, J. P., Macri, L. M., Masters, K. L., et al. 2012, *ApJS*, 199, 26
- Humphreys, E. M. L., Reid, M. J., Moran, J. M., Greenhill, L. J., & Argon, A. L. 2013, *ApJ*, 775, 13
- Jacobs, B. A., Rizzi, L., Tully, R. B., et al. 2009, *AJ*, 138, 332
- Jarrett, T. H., Chester, T., Cutri, R., et al. 2000, *AJ*, 119, 2498
- Jones, D. H., Read, M. A., Saunders, W., et al. 2009, *MNRAS*, 399, 683
- Kaiser, N., Burgett, W., Chambers, K., et al. 2010, in *Society of Photo-Optical Instrumentation Engineers (SPIE) Conference Series*, Vol. 7733, *Society of Photo-Optical Instrumentation Engineers (SPIE) Conference Series*, 0
- Karachentsev, I. D., Karachentseva, V. E., Kudrya, Y. N., Sharina, M. E., & Parnovskij, S. L. 1999, *Bull. Special Astrophys. Obs.*, 47, 5
- Karachentsev, I. D., Makarova, L. N., Makarov, D. I., Tully, R. B., & Rizzi, L. 2015a, *MNRAS*, 447, L85
- Karachentsev, I. D., Makarova, L. N., Tully, R. B., Wu, P.-F., & Kniazev, A. Y. 2014a, *MNRAS*, 443, 1281
- Karachentsev, I. D., Tully, R. B., Makarova, L. N., Makarov, D. I., & Rizzi, L. 2015b, *ApJ*, 805, 144
- Karachentsev, I. D., Tully, R. B., Wu, P.-F., Shaya, E. J., & Dolphin, A. E. 2014b, *ApJ*, 782, 4
- Lagattuta, D. J., Mould, J. R., Staveley-Smith, L., et al. 2013, *ApJ*, 771, 88
- Lavaux, G., & Hudson, M. J. 2011, *MNRAS*, 416, 2840
- Lynden-Bell, D. 1992, in *Statistical Challenges in Modern Astronomy*, ed. E. D. Feigelson & G. J. Babu, 201–220
- Lynden-Bell, D., Faber, S. M., Burstein, D., et al. 1988, *ApJ*, 326, 19
- Magoulas, C., Springob, C. M., Colless, M., et al. 2012, *MNRAS*, 427, 245
- Makarov, D., & Karachentsev, I. 2011, *MNRAS*, 412, 2498
- Makarov, D., Makarova, L., Rizzi, L., et al. 2006, *AJ*, 132, 2729
- Makarov, D., Prugniel, P., Terekhova, N., Courtois, H., & Vauglin, I. 2014, *A&A*, 570, A13
- Masters, K. L., Springob, C. M., Haynes, M. P., & Giovanelli, R. 2006, *ApJ*, 653, 861
- Mei, S., Blakeslee, J. P., Côté, P., et al. 2007, *ApJ*, 655, 144
- Morrissey, P., Conrow, T., Barlow, T. A., et al. 2007, *ApJS*, 173, 682
- Neill, J. D., Seibert, M., Tully, R. B., et al. 2014, *ApJ*, 792, 129
- Nusser, A., & Davis, M. 1995, *MNRAS*, 276, 1391
- . 2011, *ApJ*, 736, 93
- Patuarel, G., Garnier, R., Petit, C., & Marthinet, M. C. 1996, *A&A*, 311, 12
- Planck Collaboration, Ade, P. A. R., Aghanim, N., et al. 2015, *ArXiv e-prints*, arXiv:1502.01589
- Rest, A., Scolnic, D., Foley, R. J., et al. 2014, *ApJ*, 795, 44
- Riess, A. G., Macri, L., Casertano, S., et al. 2011, *ApJ*, 730, 119
- Riess, A. G., Macri, L. M., Hoffmann, S. L., et al. 2016, *ArXiv e-prints*, arXiv:1604.01424
- Rigault, M., Aldering, G., Kowalski, M., et al. 2015, *ApJ*, 802, 20
- Rizzi, L., Tully, R. B., Makarov, D., et al. 2007, *ApJ*, 661, 815
- Salo, H., Laurikainen, E., Laine, J., et al. 2015, *ApJS*, 219, 4
- Schlechter, P. 1976, *ApJ*, 203, 297
- Schlafly, E. F., & Finkbeiner, D. P. 2011, *ApJ*, 737, 103
- Schombert, J. 2007, *ArXiv Astrophysics e-prints*, astro-ph/0703646
- Sheth, K., Regan, M., Hinz, J. L., et al. 2010, *PASP*, 122, 1397
- Sorce, J. G., Courtois, H. M., & Tully, R. B. 2012a, *AJ*, 144, 133
- Sorce, J. G., Tully, R. B., & Courtois, H. M. 2012b, *ApJL*, 758, L12
- Sorce, J. G., Tully, R. B., Courtois, H. M., et al. 2014, *MNRAS*, 444, 527
- Sorce, J. G., Courtois, H. M., Tully, R. B., et al. 2013, *ApJ*, 765, 94
- Springob, C. M., Masters, K. L., Haynes, M. P., Giovanelli, R., & Marinoni, C. 2007, *ApJS*, 172, 599
- Springob, C. M., Magoulas, C., Colless, M., et al. 2014, *MNRAS*, 445, 2677
- Strauss, M. A., & Willick, J. A. 1995, *PhR*, 261, 271
- Tonry, J. L., Dressler, A., Blakeslee, J. P., et al. 2001, *ApJ*, 546, 681
- Tully, R. B. 2015a, *AJ*, 149, 54
- . 2015b, *AJ*, 149, 171
- Tully, R. B., & Courtois, H. M. 2012, *ApJ*, 749, 78
- Tully, R. B., & Fisher, J. R. 1977, *A&A*, 54, 661
- Tully, R. B., Libeskind, N. I., Karachentsev, I. D., et al. 2015, *ApJL*, 802, L25
- Tully, R. B., & Pierce, M. J. 2000, *ApJ*, 533, 744
- Tully, R. B., Scaramella, R., Vettolani, G., & Zamorani, G. 1992, *ApJ*, 388, 9
- Tully, R. B., Shaya, E. J., Karachentsev, I. D., et al. 2008, *ApJ*, 676, 184
- Tully, R. B., Courtois, H. M., Dolphin, A. E., et al. 2013, *AJ*, 146, 86
- van der Marel, R. P., Fardal, M., Besla, G., et al. 2012, *ApJ*, 753, 8
- Walker, E. S., Baltay, C., Campillay, A., et al. 2015, *ApJS*, 219, 13
- Watkins, R., & Feldman, H. A. 2015, *MNRAS*, 450, 1868
- Willick, J. A. 1994, *ApJS*, 92, 1
- Wu, P.-F., Tully, R. B., Rizzi, L., et al. 2014, *AJ*, 148, 7
- Zaritsky, D., Zabludoff, A. I., & Gonzalez, A. H. 2011, *ApJ*, 727, 116

Table 3. Summary Group Properties

Nest	N_d^{gp}	$\langle \mu \rangle^{gp}$	ϵ_μ^{gp}	d^{gp}	Abell	Gp Name
100002	161	31.01	0.02	15.9		Virgo
200009	113	36.33	0.04	184.4	A3716	
100010	112	36.45	0.04	194.7	A3558	
100001	106	34.92	0.04	96.5	A1656	Coma
100007	99	35.86	0.04	148.7	A2147	
100006	69	33.67	0.05	54.3	A1060	Hydra
100003	66	33.04	0.04	40.5	A3526	Centaurus
200015	65	31.36	0.03	18.7		Fornax
100004	62	35.47	0.06	124.3	A2199	
200007	61	35.83	0.06	146.9	A0496	

N_v	PGC1	Gl_{on}^{gp}	Gl_{at}^{gp}	SGL^{gp}	SGB^{gp}	$LogL^{gp}$	cf	σ_p	R_{2t}	V_h^{gp}	V_{gr}^{gp}	V_{ls}^{gp}
197	41220	284.09	74.41	103.0008	-2.3248	12.94	1.00	707	1.920	1156	1098	1064
52	66047	345.81	-39.39	224.6483	17.2124	14.21	9.90	1950	5.295	14072	14028	13998
55	47202	312.07	30.45	149.1678	-1.3439	14.18	7.95	1908	5.180	14414	14263	14192
136	44715	58.99	88.14	89.6226	8.1461	13.40	1.65	1045	2.839	6926	6940	6926
86	56962	30.43	44.46	108.5182	49.0878	13.77	3.30	1385	3.761	11180	11283	11273
85	31478	269.60	26.41	139.4478	-37.6063	12.73	1.14	588	1.597	3712	3490	3424
113	43296	302.20	21.74	156.2336	-11.5868	13.00	1.12	746	2.027	3550	3361	3285
49	12651	236.82	-54.80	262.8089	-40.9336	12.33	1.00	414	1.123	1457	1326	1319
81	58265	63.86	43.84	71.5103	49.7851	13.41	2.26	1057	2.871	9177	9348	9369
54	15524	209.07	-36.70	296.2707	-55.3232	13.28	2.37	954	2.591	9904	9794	9803

V_{cmb}^{gp}	V_{mod}^{gp}	V_{rms}	M_{12}^{bw}	M_{12}^L	LDC	HDC	2M++	M&K	Icnt
1485	1491	670	935.000	705.000	852	716	0	5066891	1
13924	14434	916	4750.000	14800.001	0	0	3385	0	2834
14697	15265	1002	4950.000	13900.000	0	0	2182	0	2551
7195	7331	886	2120.000	2280.000	890	734	1952	0	2493
11270	11603	1261	7080.000	5310.000	0	0	2138	0	2652
4055	4099	648	585.000	407.000	712	592	1122	5066799	487
3834	3873	822	1440.000	831.000	881	722	1107	5066908	441
1357	1362	301	107.000	141.000	391	235	2	5066701	843
9202	9424	740	1880.000	2360.000	1134	936	1858	0	2642
9851	10106	529	915.000	1730.000	307	294	3653	0	2181

Table 4. Individual Galaxy Properties

PGC	d	N_d	$\langle \mu \rangle$	ϵ_μ	C	T	L	M	S	N	H	I	F	P	μ_{cf2}	ϵ_{cf2}^μ	SN	N_{sn}	μ_{sn}	μ_{spit}	ϵ_{spit}^μ	μ_{6df}	ϵ_{6df}^μ	M_t	
4	50.58	1	33.52	0.40							H				33.52	0.40		0	0.00	0.00	0.00	0.00	0.00		
27	150.66	1	35.89	0.50										P	0.00	0.00		0	0.00	0.00	0.00	0.00	35.89	0.50	3.7
40	116.95	1	35.34	0.50										P	0.00	0.00		0	0.00	0.00	0.00	0.00	35.34	0.50	3.0
51	240.99	1	36.91	0.50										P	0.00	0.00		0	0.00	0.00	0.00	0.00	36.91	0.50	2.8
55	73.79	1	34.34	0.40							H				34.34	0.40		0	0.00	0.00	0.00	0.00	0.00		
64	211.84	1	36.63	0.50										P	0.00	0.00		0	0.00	0.00	0.00	0.00	36.63	0.50	0.0
66	182.81	1	36.31	0.50										P	0.00	0.00		0	0.00	0.00	0.00	0.00	36.31	0.50	0.0
70	117.49	1	35.35	0.40							H				35.35	0.40		0	0.00	0.00	0.00	0.00	0.00		
76	97.72	1	34.95	0.40							H				34.95	0.40		0	0.00	0.00	0.00	0.00	0.00		
82	114.82	1	35.30	0.50										P	0.00	0.00		0	0.00	0.00	0.00	0.00	35.30	0.50	0.8

RA_J	Dec_J	G_{lon}	G_{lat}	SGL	SGB	T_y	A_{sf}	B_t	K_s	V_h	V_{gsr}	V_{ls}	V_{cmb}	V_{mod}	Name	Nest	N_d^{gp}	$\langle \mu \rangle^{gp}$	ϵ_μ^{gp}	d^{gp}
000003.5	+230515	107.8322	-38.2729	316.0587	18.4514	5.0	0.331	16.88	0.00	4458	4638	4706	4109	4154	AGC331060	202766	1	33.52	0.40	50.6
000023.5	-065610	89.6452	-66.4507	285.8972	11.1231	2.0	0.129	16.06	0.00	11311	11405	11445	10959	11275		0	1	35.89	0.50	150.7
000035.6	-014547	95.1366	-61.8596	290.9658	12.5924	-1.0	0.132	15.11	0.00	7277	7388	7434	6919	7045		209793	1	35.34	0.50	116.9
000035.8	-403432	337.6665	-72.9440	254.0322	-0.2359	0.0	0.037	16.93	0.00	15015	14983	14980	14771	15342	PGC000051	201987	1	36.91	0.50	241.0
000037.4	+333603	110.9496	-28.0856	327.0998	19.7763	5.9	0.183	17.04	0.00	4779	4979	5052	4454	4507	UGC12898	0	1	34.34	0.40	73.8
000052.3	-355037	350.7982	-76.1593	258.4801	1.3810	-5.0	0.042	15.53	0.00	15596	15582	15585	15331	15946		200033	11	36.25	0.15	178.1
000053.2	-355911	350.3084	-76.0782	258.3474	1.3282	-5.0	0.046	15.80	0.00	14996	14981	14985	14731	15300		200033	11	36.25	0.15	178.1
000056.1	+202016	107.1780	-40.9837	313.2487	17.7662	5.8	0.282	15.61	11.26	6800	6974	7040	6447	6557	UGC12900	209949	1	35.35	0.40	117.5
000058.9	+285441	109.8059	-32.6707	322.1728	19.1316	3.0	0.178	14.82	11.01	6920	7112	7183	6583	6698	UGC12901	209247	1	34.95	0.40	97.7
000106.0	-535931	318.5468	-61.5837	241.4720	-4.9970	-1.3	0.050	14.67	0.00	9426	9344	9324	9251	9476		200218	9	36.21	0.17	174.2

Abell	Gp Name	N_v	PGC1	G_{lon}^{gp}	G_{lat}^{gp}	SGL^{gp}	SGB^{gp}	$LogL^{gp}$	cf	σ_p	R_{2t}	V_h^{gp}	V_{gsr}^{gp}	V_{ls}^{gp}	V_{cmb}^{gp}	V_{mod}^{gp}	V_{rms}	M_{12}^{bw}	M_{12}^L	LDC	HDC	2M++	M&K	Icnt
		2	120	108.41	-37.98	316.5396	18.1559	11.32	1.15	170	0.460	4353	4533	4601	4005	4048	25		9.750	0	0	0	0	0
		1	27	89.65	-66.45	285.8972	11.1231					11311	11405	11445	10959	11275			0	0	0	0	0	0
		1	40	95.14	-61.86	290.9657	12.5924	10.98	1.66	126	0.341	7277	7388	7434	6919	7045			0	0	0	0	0	0
		2	142	337.01	-72.84	253.8705	-0.3818	12.55	8.84	502	1.364	14986	14953	14950	14743	15315	132		253.000	0	0	0	0	0
		1	55	110.95	-28.09	327.0998	19.7763					4779	4979	5052	4454	4507			0	0	0	0	0	0
A2717		25	72642	356.24	-75.69	258.8940	2.7238	14.10	8.84	1788	4.857	15000	14991	14996	14729	15300	1582	17100.000	11400.000	0	0	0	3084	0
A2717		25	72642	356.24	-75.69	258.8940	2.7238	14.10	8.84	1788	4.857	15000	14991	14996	14729	15300	1582	17100.000	11400.000	0	0	0	3084	0
		1	70	107.18	-40.98	313.2488	17.7663	10.95	1.53	122	0.332	6800	6974	7040	6447	6557			3.650	0	0	0	0	0
		1	76	109.81	-32.67	322.1729	19.1316	11.09	1.54	139	0.376	6920	7112	7183	6583	6698			5.310	1536	0	0	0	0
		7	211	317.61	-61.47	241.3354	-5.4383	12.52	2.84	489	1.328	10418	10334	10313	10245	10520	635	832.000	233.000	5	0	0	3377	0